How to cite: *Angew. Chem. Int. Ed.* **2023**, *62*, e202311832
doi.org/10.1002/anie.202311832

Surface Chemistry | Hot Paper

Self-Assembled Monolayers of N-Heterocyclic Olefins on Au(111)

*Iris Berg, Luca Schio, Justus Reitz, Elena Molteni, Linoy Lahav, Carolina Gutiérrez Bolaños, Andrea Goldoni, Cesare Grazioli, Guido Fratesi, Max M. Hansmann, Luca Floreano, and Elad Gross**

Abstract: Self-assembled monolayers (SAMs) of N-heterocyclic olefins (NHOs) have been prepared on Au(111) and their thermal stability, adsorption geometry, and molecular order were characterized by X-ray photoelectron spectroscopy, polarized X-ray absorption spectroscopy, scanning tunneling microscopy (STM), and density functional theory (DFT) calculations. The strong σ-bond character of NHO anchoring to Au induced high geometrical flexibility that enabled a flat-lying adsorption geometry via coordination to a gold adatom. The flat-lying adsorption geometry was utilized to further increase the surface interaction of the NHO monolayer by backbone functionalization with methyl groups that induced high thermal stability and a large impact on work-function values, which outperformed that of N-heterocyclic carbenes. STM measurements, supported by DFT modeling, identified that the NHOs were self-assembled in dimers, trimers, and tetramers constructed of two, three, and four complexes of NHO–Au-adatom. This self-assembly pattern was correlated to strong NHO–Au interactions and steric hindrance between adsorbates, demonstrating the crucial influence of the carbon-metal σ-bond on monolayer properties.

Introduction

The strong affinity of N-heterocyclic carbene (NHC) ligands to metals, metal-oxides, and semimetals enabled the formation of NHC-based self-assembled monolayers (SAMs) on a variety of surfaces.[1] The thermal stability[2] and synthetic versatility[3] of NHCs have made NHC-based SAMs a viable alternative to thiol-based monolayers. Due to these advantages, NHC-based SAMs were applied as (bio)sensors,[3b,g,k,4] ligands for nanoparticles and clusters,[1e,2c,3a,5] molecular probes for surface reactivity,[6] modifiers for electronic devices,[3d,7] corrosion inhibitors,[8] and co-catalysts.[3a,9]

NHCs are well-established ligands in transition metal chemistry and homogeneous catalysis. While σ-donation is the most important component of metal-ligand binding, NHCs also function as π-accepting ligands.[10] Their σ-donor ability makes them suitable surface binders for late-transition metals, such as gold.[2a,11] Self-assembly of various classes of NHCs was investigated to identify the influence of the carbene ring properties on surface-anchoring. This includes carbenes such as cyclic (alkyl)(amino)carbenes (CAAC)[3c,12] with a single nitrogen atom in the carbene heterocycle, and triazolone-based compounds,[13] such as nitron.[14] However, in all aforementioned ligands, surface-anchoring was induced via the carbene carbon thus combining both σ-donation and π-back-donation capabilities and restricting the disentangling of these two effects.

N-heterocyclic olefins (NHOs) represent a different class of carbon-based ligands that are formally composed of an alkylidene moiety (CH_2) appended to the NHC (Scheme 1a).[15–17] NHOs can be represented by a neutral as well as a zwitterionic mesomeric Lewis structure (Scheme 1a).[18] The stabilization of the positive charge by the aromatic imidazolium moiety, makes NHOs highly polarized towards the exocyclic carbon atom thus leading to a strong σ-donor, with negligible π-accepting character. The pronounced difference between these overall donor effects is reflected by the low Tolman electronic parameter (TEP) of NHOs compared to NHCs [TEP (NHO) ≈ 2025–2030 cm^{-1}; TEP (NHC) ≈ 2040–2051 cm^{-1}].[19] Due to these electronic characteristics, NHOs and their derivatives have found broad application in transition metal- and organo-catalysis,[20] main-group,[21] and coordination chemistry,[22] or polymer chemistry.[23] However, the utilization of NHOs as

[*] I. Berg, L. Lahav, Prof. E. Gross
Institute of Chemistry and The Center for Nanoscience and Nanotechnology, The Hebrew University, Jerusalem 91904 (Israel)
E-mail: elad.gross@mail.huji.ac.il
Dr. L. Schio, Dr. C. Grazioli, Dr. L. Floreano
CNR-IOM, Laboratorio TASC, Basovizza SS-14, Km 163.5, Trieste 34012 (Italy)
J. Reitz, Prof. M. M. Hansmann
Technische Universität Dortmund, Fakultät für Chemie und Chemische Biologie, Otto-Hahn-Str. 6, 44227 Dortmund (Germany)
Dr. E. Molteni, Prof. G. Fratesi
Dipartimento di Fisica "Aldo Pontremoli" Università degli Studi di Milano, Via Celoria 16, 20133 Milano (Italy)
C. G. Bolaños, Dr. A. Goldoni
Elettra-Sincrotrone Trieste S.C.p.A, Basovizza SS-14, Km 163.5, Trieste 34149 (Italy)

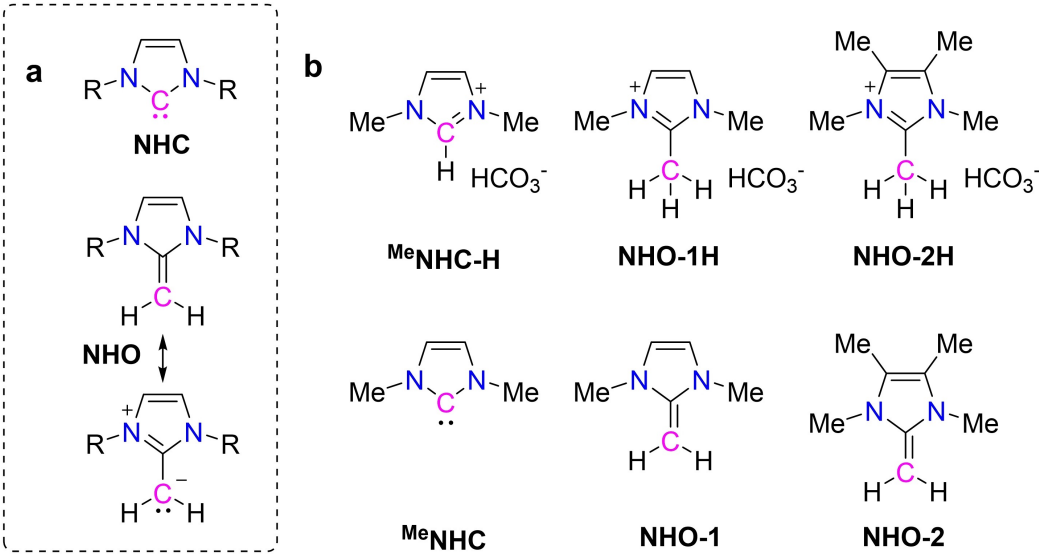

Scheme 1. a) Molecular structures of NHCs and NHOs. b) Molecular structures of 1,3-dimethyl imidazolium hydrogen carbonate (^{Me}NHC-H), 1,2,3-trimethyl imidazolium hydrogen carbonate (NHO-1H), and 1,2,3,4,5-pentamethyl imidazolium hydrogen carbonate (NHO-2H) that were used as precursors for vapor deposition of ^{Me}NHC, NHO-1 and NHO-2, respectively, on Au(111).

surface ligands that can decouple the σ-donation and π-back-donation properties was not yet explored.

In this work we show that NHOs derived from their protonated imidazolium salts (NHO-1/2H) (Scheme 1b) are self-assembled on Au(111) via σ-bond interaction with Au-adatom, forming a pattern of dimers, trimers and tetramers that are constructed of NHO–Au-adatom complexes. The σ-bond character provided geometrical flexibility, enabling a flat-lying adsorption geometry that induced high thermal stability and substantially reduced the substrate work-function. The high flexibility of surface-anchored NHOs enabled to further increase their surface interaction by backbone functionalization that also resulted in an improved thermal stability.

Results and Discussion

The self-assembly of NHO-1 and NHO-2 on Au(111) were studied and the properties of NHO monolayers were compared to that of ^{Me}NHC, which serves based on its structural similarity as a carbene reference to NHO-1 (Scheme 1b). NHO-1 and NHO-2 were chosen for this study to identify the impact of backbone functionalization on NHO self-assembly.[24] NHO-1 and NHO-2 are highly air-sensitive compounds, therefore we were interested in air-stable precursors for their in situ generation. In order to find a pathway to generate the desired NHOs on the surface without addition of external base we selected bench-stable hydrogen carbonate salts as precursors, a procedure established for the generation of carbenes on surfaces.[2b,3b,e,25] It should be noted that NHO formation and self-assembly can be also achieved by the addition of an external base, which will be described further below.

Based on this procedure, ^{Me}NHC as well as NHO-1 and NHO-2 were vapor deposited under ultrahigh vacuum (UHV) conditions on Au(111) while using 1,3-dimethyl imidazolium hydrogen carbonate (^{Me}NHC-H), 1,2,3-trimethyl imidazolium hydrogen carbonate (NHO-1H) and 1,2,3,4,5-pentamethyl imidazolium hydrogen carbonate (NHO-2H) as precursors for ^{Me}NHC, NHO-1, and NHO-2, respectively (for additional synthetic details, see experimental section and Figures S1–S12). Vapor deposition was performed by *in-vacuo* sublimation of the solid precursor at 350 K from a Knudsen cell with a boron nitride crucible.[3b,e] The anchoring geometry and thermal stability of the SAMs were characterized using X-ray photoelectron spectroscopy (XPS) and polarized near-edge X-ray absorption fine structure (NEXAFS) measurements (performed at the ALOISA beamline of the ELETTRA synchrotron facility in Trieste, Italy).[26]

N1s XPS signals of NHO-1 and NHO-2 on Au(111) were acquired and are shown in Figure 1a and 1b, respectively. XPS measurements were performed following annealing to 150 °C to remove physisorbed residues (Figure S13). The N1s spectra of NHO-1 and NHO-2 was fit to a Gaussian centered at 402.2 and 402.0 eV, respectively (Figure 1a and 1b). A shoulder at lower binding energy was probed for NHO-1 and assigned to physisorbed residues,[27] which desorbed upon further annealing. To compare the properties of NHO monolayers with that of NHCs, ^{Me}NHC was deposited on Au(111) under UHV conditions and characterized by XPS measurements. The N1s XPS spectrum of ^{Me}NHC (Figure 1c) was fit by one main Gaussian that was centred at 401.2 eV, in agreement with previous observations.[25c] A minor Gaussian was located at 402.2 eV and assigned to protonated nitrogen.[28]

The obtained results demonstrate that NHOs can be self-assembled on Au(111) to form a stable monolayer. The

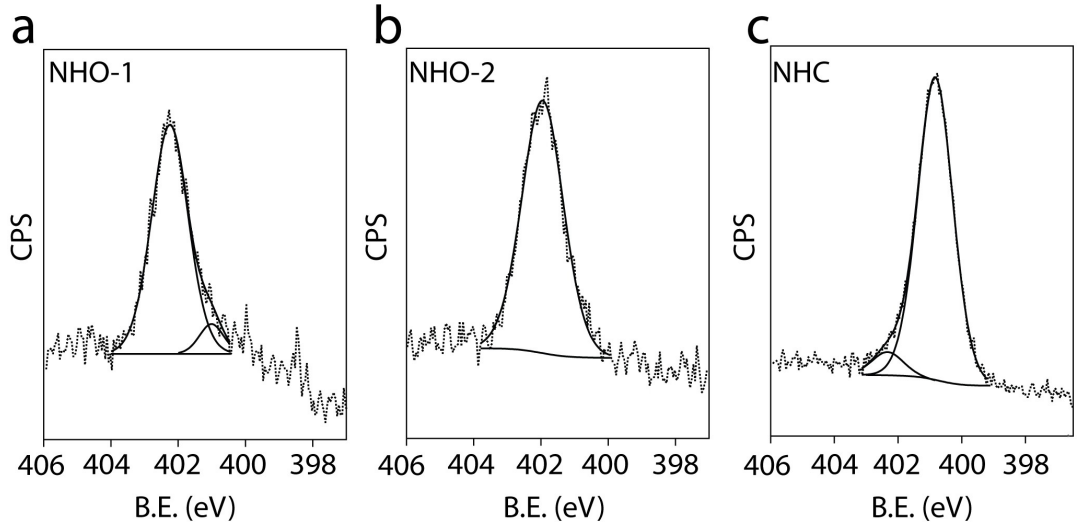

Figure 1. N1s XPS signals of (**a**) NHO-1 (**b**) NHO-2 and (**c**) ^{Me}NHC on Au(111).

N1s XPS signals of the two NHOs were shifted towards higher binding energies than that of ^{Me}NHC, indicative of a partial positive charge on the nitrogen atoms, which was correlated to the zwitterionic structure of NHO.[29] The peak area of NHO-1 and NHO-2 was lower by 53 and 52 %, respectively, than that of ^{Me}NHC. The lower surface density of NHOs can be linked to their larger molecular footprint and stronger surface interactions, as will be further detailed in STM measurements and DFT calculations.

Nitrogen K-edge NEXAFS measurements were conducted to elucidate the anchoring geometry of NHOs by comparing their p- and s-polarized NEXAFS spectra (marked by solid and dotted lines, respectively, in Figure 2). NEXAFS measurements of NHO-1 and NHO-2 were performed after annealing to 150 and 200 °C, respectively, to remove all physisorbed residues. Nitrogen K-edge NEXAFS spectrum of NHO-1 (Figure 2a) showed a dominant π* transition at 401.8 eV, correlated to N1s→$\pi^*_{(N=C)}$,[29] and two smaller peaks positioned at 398.8 eV and 399.8 assigned to N1s→$\pi^*_{(N=C=C)}$ and N1s→$\pi^*_{(N-C=C)}$, respectively.[29–30] Enhanced signal was obtained at p-polarization in the π* range and implies that the imidazole ring adopted a flat-lying adsorption geometry with respect to the surface normal (see experimental section for details). A continuum of transitions was measured in the σ* region (404–415 eV), correlated to N1s→σ* transitions.[29] In the σ* region, the intensity of the spectrum at s-polarization was higher than that of p-polarization. The opposite dichroism in the σ* region is an additional indication for the preference towards a flat-lying orientation with respect to the surface.

Nitrogen K-edge NEXAFS spectra of NHO-2 on Au(111) showed a similar pattern to the one detected for NHO-1 with a dominant N1 s→$\pi^*_{(N=C)}$ transition in the π* region, centered at 401.8 eV, and a clear positive dichroism characteristic of a flat-lying geometry (Figure 2b). N1s→σ* transitions were detected in the σ* region, and displayed an

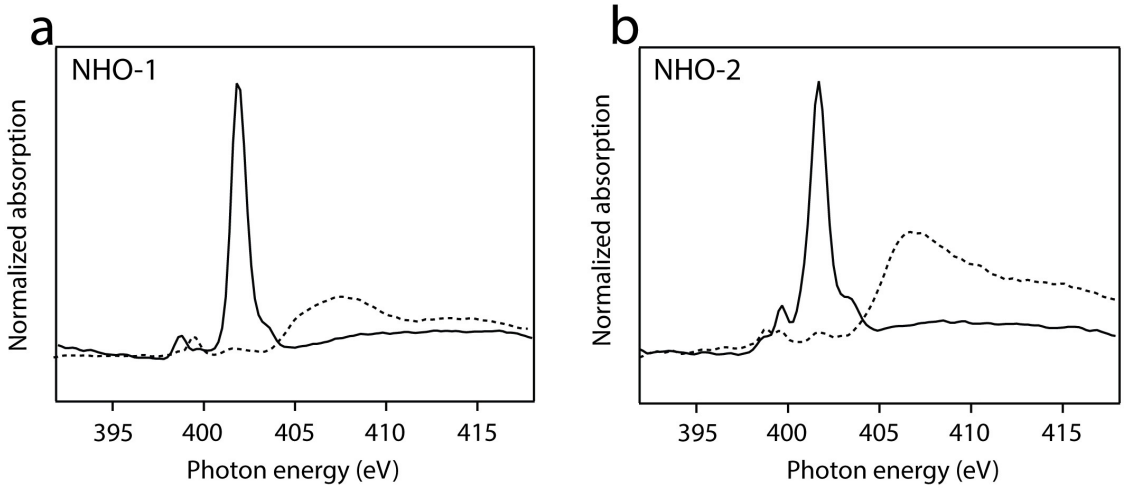

Figure 2. Nitrogen K-edge NEXAFS spectra measured at p- and s-polarizations (solid and dotted lines, respectively) of (a) NHO-1 and (b) NHO-2.

opposite dichroism trend comparing to the π* region, which further specifies that the surface-anchored molecules were adsorbed in a flat-lying geometry. Small transitions were detected at 399.8 and 403.4 eV and correlated to a more oxidized species (Figure 2b).[3e,31] Nitrogen and carbon K-edge NEXAFS spectra of ^{Me}NHC showed similar dichroism, which specified a flat-lying adsorption geometry (Figure S14–S15), in accordance with previous publications.[11c,25c]

DFT structural optimizations starting with olefinic (planar) NHO identified an optimal adsorption of NHO-1 (Figure 3a–b) and NHO-2 (Figure 3c–d) on Au(111) and Au-adatoms with a flat-lying adsorption geometry (Table S1). The adsorption energies of NHO-1 and NHO-2 on a Au-adatom were −2.73 and −3.00 eV, respectively, while values lower by ~0.7 eV were calculated for NHOs adsorption on Au(111). It should be noted that the energetic stabilization that stems from adsorption on an adatom (ΔE = 0.69 eV for NHO-2) does not fully compensate for the energetic cost of adatom formation on terrace sites (0.79 eV). Thus, it is hypothesized that NHO-adatom formation was initially induced on step sites, as validated in STM images that showed large meandering and indentation of monoatomic steps following adsorption of NHOs (Figure S16). The adsorption energy of flat-lying ^{Me}NHC on Au-adatom was −2.72 eV, which is in good agreement with a previous study for NHCs,[32] although a larger value was also reported.[11c] The calculations hence show that NHO-1 and ^{Me}NHC have similar adsorption energies, while NHO-2 has a higher adsorption energy due to backbone functionalization that induced stronger surface interactions.

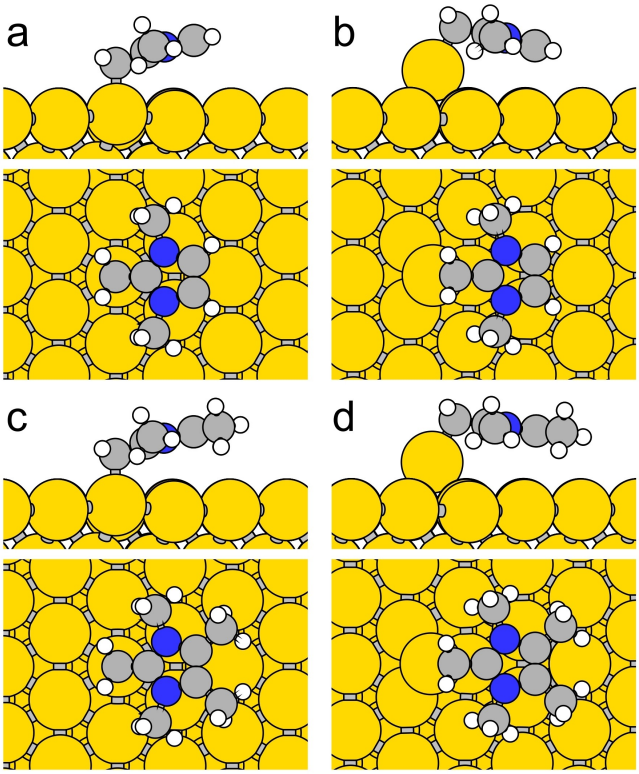

Figure 3. Calculated optimized adsorption geometries for NHO-1 (a–b), and NHO-2 (c–d) on a terrace (a, c), and on a Au-adatom (b, d).

DFT analysis of bond lengths and bond angles of NHO-1 and NHO-2 was performed to elucidate the ylidic versus olefinic character of surface-anchored NHOs (Scheme 1). The bond length of the carbene carbon with the CH_2 carbon (denoted as C1 and C6, respectively, in Figure S17) was increased by ca. 0.1 Å (NHO-1: 1.364 Å to 1.444 Å; NHO-2: 1.365 Å to 1.447 Å) upon adsorption of both NHO-1 and NHO-2 on a Au-adatom (Table S2). In addition, the calculated bond angle of C1–C6–Au was 107° and 110° for surface-anchored NHO-1 and NHO-2, respectively. Both observations indicate that the CH_2 carbon in surface-anchored NHO is sp^3 hybridized, which is indicative of NHO adsorption in ylidic rather than in olefinic structure. This coordination mode is also in agreement with the homogeneous, molecular Au complexes of NHOs showing an end-on coordination to the metal center with a Au–C bond length of 2.087(3) Å,[19a] in a similar range to the calculated values for the Au-surface bound species (2.124 Å to 2.135 Å; Table S2). Analysis of the electron density displacement upon adsorption (Figure S18) highlights an accumulation of charge density between the C6 atom and the Au-adatom with nearly cylindrical symmetry around the Au–C bond, together with a depletion of π charge within the molecule and a minor accumulation of charge in the backbone plane. A strong bonding with the Au-adatom is also recognized by analyzing the electronic density of states projected on atomic orbitals[33] showing a large hybridization of the highest occupied molecular orbitals (HOMO) and HOMO-1, both having π symmetry but especially a strong amplitude at the C6 atom, with surface states (Figure S19). These results further rationalize the high adsorption energy of NHOs on Au.

The thermal stabilities of NHO-1, NHO-2 and ^{Me}NHC were analysed by recording their N1s XPS signal following annealing (Figure 4 and Figure S20). Comparative analysis of the normalized N1s XPS peak area demonstrated the improved thermal stability of NHO-1 and NHO-2 over that of ^{Me}NHC (Figure 4). The N1s XPS signal of ^{Me}NHC was reduced by 90 % after annealing to 300 °C, while that of NHO-1 and NHO-2 were reduced by 34 and 25 %, respectively. NHO-2 showed improved thermal stability, and nitrogen signal was detected even after annealing to 400 °C, and preserved its original peak pattern up to 300 °C (Figure S20). Further annealing of NHO-2 to 350 and 400 °C led to significant peak shifts toward lower binding energies, which may indicate decomposition of the molecules and formation of pyridine species.[34] The improved thermal stability of NHO monolayers can be attributed to their strong σ donating properties.[15] The enhanced stability of NHO-2, in comparison to NHO-1, is correlated to stronger surface interactions that are induced by the methyl groups on its backbone.

To examine the role of the precursor in NHO self-assembly we also investigated a hydrogen carbonate free synthetic approach and an independent synthetic strategy applying an external base. Self-assembled monolayers of NHO-1 and NHO-2 were prepared by using 1,2,3-trimethyl

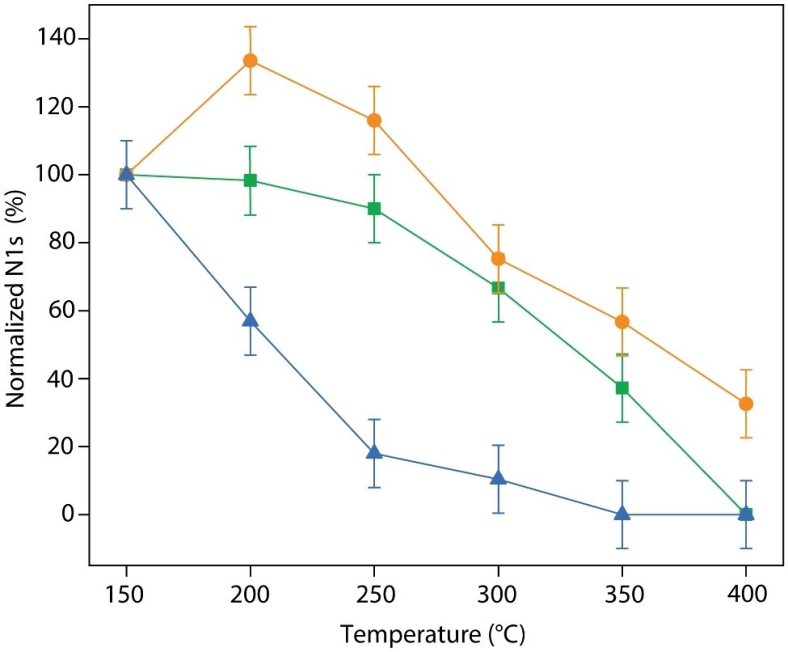

Figure 4. Normalized N1s XPS peak area of NHO-1 (green), NHO-2 (orange) and ^{Me}NHC (blue).

imidazolium and 1,2,3,4,5-pentamethyl imidazolium salts, both containing iodide anions as precursors. Deprotonation was induced by potassium *tert*-butoxide immersed in THF (experimental details are provided in the SI). N1s XPS signal of NHO monolayers that were self-assembled on Au film and prepared while using halide-imidazolium precursors showed an overall similar pattern to that of NHO monolayers prepared via UHV deposition of imidazolium hydrogen carbonate precursors (Figure S22). The N1s/Au4f XPS peak area ratios of NHO-1 and NHO-2, which were prepared by base-induced deprotonation of imidazolium iodide precursors, were comparable to that of NHC monolayers that were prepared by base-induced deprotonation.[3b,e]

Deprotonation of 1,2,3,4,5-pentamethyl imidazolium hydrogen carbonate precursor (NHO-2H) for the formation of NHO-2 monolayer was also demonstrated under liquid phase conditions. NHO-2 monolayer was prepared on a Au film, following annealing of THF-solvated NHO-2H at 70 °C. The N1s XPS signal of NHO that was prepared by using solvated 1,2,3,4,5-pentamethyl imidazolium hydrogen carbonate resembled the pattern of the sample prepared by 1,2,3,4,5-pentamethyl imidazolium iodide precursor (Figure S22). These experiments further validate that NHO monolayers can be prepared by using NHO precursors with either halide or hydrogen carbonate anions and deprotonation can be achieved with a strong base or via annealing, respectively.

Slow exchange of the imidazole-CH_3 protons for imidazole-CD_3 was observed in CD_3CN solution for the hydrogen carbonate salts and indicated the possibility to form the olefin as a transient intermediate (Figure S23 and S24). Heating the hydrogen carbonate precursors NHO-1/2H under vacuum (10^{-3} mbar) did not induce sufficient amounts of NHOs to be detected by NMR, but mostly resulted in sublimation of the salts. These results indicate that mechanistically, deprotonation is either characterized with a very low efficiency (which is sufficient for surface deposition) or that deprotonation is further facilitated by surface interactions.

Low-energy XPS measurements were conducted to quantify the electronic effects of NHO monolayers on the work function of Au(111). Changes in the work function values of -1.9 ± 0.1, -2.4 ± 0.1 and -2.1 ± 0.1 V were measured for NHO-1, NHO-2 and ^{Me}NHC, respectively (Figure S25). These results show that all three molecules significantly reduce the work function of Au, as expected for molecules with high σ-donation affinity and as previously demonstrated for NHC monolayers.[7a] NHO-2, which was postulated to be a better σ-donor in comparison to ^{Me}NHC and NHO-1, induced a noticeable decrease in the work function value that outperformed that of NHCs. It should be noted that the surface density of NHOs was lower by 50 % in comparison to that of NHCs. Thus, the normalized effect of NHOs is larger in comparison to NHCs, in line with their strong donor characteristics.

The self-assembly pattern of NHOs on Au(111) was imaged using STM measurements. High mobility of both NHO-1 and NHO-2 was detected, which prevented their high-resolution imaging at room temperature (Figure S16). Low-temperature (130 K) STM imaging of NHO-1 (Figure 5a–c) and NHO-2 (Figure 5d–f) on Au(111) revealed that NHOs were self-assembled in units of trimers and tetramers structures. The average height of isolated NHO-1 and NHO-2 was 105 and 80 pm, respectively, which is indicative of a flat-lying adsorption geometry. For both NHOs, a similar self-assembly pattern was observed, though lower surface density was identified for NHO-1, possibly

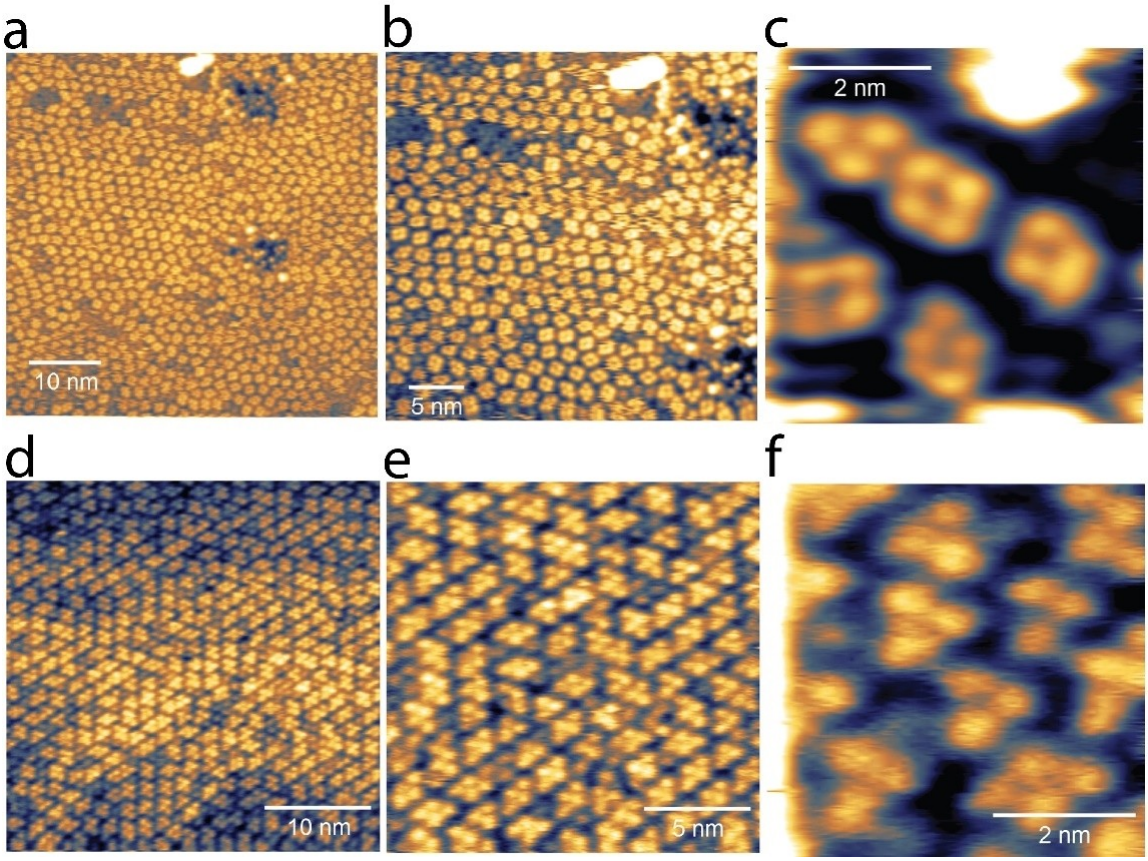

Figure 5. a–b. STM images of NHO-1 on Au(111) (130 K, +1.3 V, 0.2 nA). c. High resolution STM image of trimers and tetramers of NHO-1 (130 K, +1.6 V, 0.25 nA). d–e. STM images of NHO-2 on Au(111) (130 K, +1.3 V, 0.2 nA). f. High resolution STM image of trimers and tetramers of NHO-2 (130 K, +1.0 V, 0.2 nA).

correlated to physisorbed species that limited the formation of a high surface density monolayer. In the case of NHO-1, tetramers equally formed a square or a rhombic shape (Figure 5c), while tetramers were mostly detected in stretched rhombic shape for NHO-2 (Figure 5f).

DFT simulations were conducted to elucidate the self-assembly patterns of NHOs. The adsorption patterns of NHO-2-Au-adatom complexes for the formation of coupled dimers (Figure 6a), trimers (Figure 6b) and tetramers (Figure 6c) were simulated and fit well the experimental STM images (Figures 6d–6f). The simulations were performed for NHO-2, and very similar patterns are expected for NHO-1, according to the resemblance of energetics, as listed in Table S1.

The calculations show that two, three and four NHO–Au-adatom complexes can self-assemble while gaining 0.07–0.08 eV/molecule in forming dimers, trimers, or tetramers with Au-adatom per NHO (see models in Figure S26). Conversely, the adsorption of a second NHO-2 molecule on the same Au-adatom is less favorable, by 0.78 eV, with respect to adsorption on a separate adatom in a dimer. While the closely squared tetramers can be attributed to four NHO–Au complexes (Figure 6c and 6f), the stretched rhombic tetramers better fit the two dimers scenario (Figure 6a and 6d). In fact, the latter configuration is also stable, although with a lower energy gain of 0.02 eV/molecule with respect to isolated NHO–Au-adatom complexes (see Table S1). The observation that stretched tetramers are mostly observed in large scale images (Figure 5d and 5e), may be attributed to activation barriers in fusing two dimers or to intermolecular interactions among adjacent supramolecular complexes that are neglected in present calculations. The absence of peripheral methyl groups in NHO-1 supramolecular complexes, as well as the overall lower surface density, favors a larger mobility, hence explaining the larger variety of tetrameric aggregates.

It was previously demonstrated that ^{Me}NHC molecules are self-assembled on Au surface and form dimers and trimers that are linked via a single Au-adatom.[11c] This assembly pattern is different than the self-assembly of NHOs that involve the assembly of NHO–Au-adatom complexes, in which each NHO is coordinated to Au-adatom.[11c,d] This distinct self-assembly pattern of NHOs is correlated to strong NHO–Au interactions and steric hindrance between adsorbates that lead to adsorption geometries that prevent the assembly of two NHO molecules on a single Au-adatom.

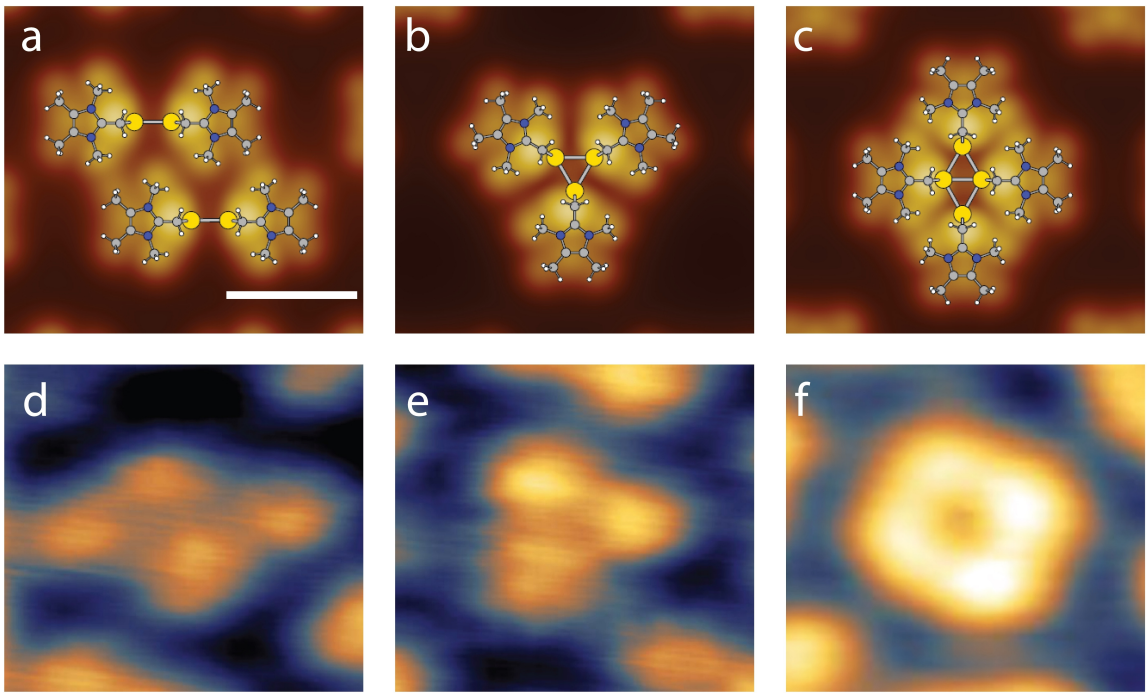

Figure 6. Simulated STM images of (a) pair of dimers, (b) trimers, and (c) tetramers of NHO-2-Au-adatom complexes and corresponding STM images of NHO-2 (d and e) and NHO-1 (f). Scale bar equals 1 nm.

Conclusion

In this work we demonstrate that NHOs form thermally stable, chemisorbed monolayers on Au(111). The monolayers were characterized with improved thermal stability, and larger effect on the work function that, for methyl-functionalized NHO-2, surpass that of ^{Me}NHC. NHOs were found to adsorb in a flat-lying adsorption geometry on a Au-adatom via end-on carbon coordination. At room temperature, the molecules were self-assembled in dimers, trimers and tetramers, constructed of two, three, and four NHO–Au-adatom complexes, respectively. The improved thermal stability of NHOs on Au(111) and their impact on work function properties demonstrate the crucial role of the surface-anchoring CH_2-group on the molecular flexibility that yielded optimized adsorption geometry. The molecular flexibility enabled to utilize NHO backbone functionalization to further improve the thermal stability and the impact on work function. By analyzing the surface properties of NHO monolayers, this work demonstrates the critical role of the surface-anchoring carbon species and its impact in tuning the surface properties of self-assembled monolayers.

Acknowledgements

This research was supported by the European Research Council (ERC) under the European Union's Horizon 2020 and Horizon Europe research and innovation program (Grant Agreement No. 802769, ERC Starting Grant "MapCat" and Grant Agreement No. 101077332, ERC Starting Grant "CC-CHARGED"). I. B. acknowledges the Clore Israel Foundation, and the Harvey M. Krueger Family Center for Nanoscience and Nanotechnology for their financial support. L.L acknowledges Harvey M. Krueger Family Center for Nanoscience and Nanotechnology for their financial support. This project has received funding from the European Union's Horizon 2020 and Horizon Europe research and innovation program under grant agreement No. 101007417 and 101077332 having benefited from the access to OSMOS STM lab provided by CNR-IOM in Trieste and by the Physics Department of the University of Milan for theoretical support, within the framework of the NFFA-Europe Pilot Transnational Access Activity, proposal ID443. We acknowledge the CINECA award under the ISCRA initiative, for the availability of high performance computing resources and support.

Conflict of Interest

The authors declare no conflict of interest.

Data Availability Statement

The data that support the findings of this study are available from the corresponding author upon reasonable request.

Keywords: N-Heterocyclic Olefins · Scanning Tunneling Microscopy · Self-Assembled Monolayers · Surface Chemistry · X-Ray Absorption Spectroscopy

[1] a) A. V. Zhukhovitskiy, M. J. MacLeod, J. A. Johnson, *Chem. Rev.* **2015**, *115*, 11503–11532; b) C. A. Smith, M. R. Narouz, P. A. Lummis, I. Singh, A. Nazemi, C. H. Li, C. M. Crudden, *Chem. Rev.* **2019**, *119*, 4986–5056; c) M. Koy, P. Bellotti, M. Das, F. Glorius, *Nat. Catal.* **2021**, *4*, 352–363; d) G. Kaur, R. L. Thimes, J. P. Camden, D. M. Jenkins, *Chem. Commun.* **2022**, *58*, 13188–13197; e) H. Shen, G. L. Tian, Z. Xu, L. Z. Wang, Q. Y. Wu, Y. H. Zhang, B. K. Teo, N. F. Zheng, *Coord. Chem. Rev.* **2022**, *458*, 214425; f) J. J. Navarro, M. Das, S. Tosoni, F. Landwehr, J. P. Bruce, M. Heyde, G. Pacchioni, B. Roldan Cuenya, F. Glorius, *J. Am. Chem. Soc.* **2022**, *144*, 16267–16271.

[2] a) C. M. Crudden, J. H. Horton, I. I. Ebralidze, O. V. Zenkina, A. B. McLean, B. Drevniok, Z. She, H. B. Kraatz, N. J. Mosey, T. Seki, E. C. Keske, J. D. Leake, A. Rousina-Webb, G. Wu, *Nat. Chem.* **2014**, *6*, 409–414; b) D. T. Nguyen, M. Freitag, M. Korsgen, S. Lamping, A. Ruhling, A. H. Schafer, M. H. Siekman, H. F. Arlinghaus, W. G. van der Wiel, F. Glorius, B. J. Ravoo, *Angew. Chem. Int. Ed.* **2018**, *57*, 11465–11469; c) J. F. DeJesus, L. M. Sherman, D. J. Yohannan, J. C. Becca, S. L. Strausser, L. F. P. Karger, L. Jensen, D. M. Jenkins, J. P. Camden, *Angew. Chem. Int. Ed.* **2020**, *59*, 7585–7590.

[3] a) A. Ferry, K. Schaepe, P. Tegeder, C. Richter, K. M. Chepiga, B. J. Ravoo, F. Glorius, *ACS Catal.* **2015**, *5*, 5414–5420; b) C. M. Crudden, J. H. Horton, M. R. Narouz, Z. J. Li, C. A. Smith, K. Munro, C. J. Baddeley, C. R. Larrea, B. Drevniok, B. Thanabalasingam, A. B. McLean, O. V. Zenkina, I. I. Ebralidze, Z. She, H. B. Kraatz, N. J. Mosey, L. N. Saunders, A. Yagi, *Nat. Commun.* **2016**, *7*, 12654; c) A. V. Zhukhovitskiy, M. G. Mavros, K. T. Queeney, T. Wu, T. Van Voorhis, J. A. Johnson, *J. Am. Chem. Soc.* **2016**, *138*, 8639–8652; d) S. Dery, S. Kim, G. Tomaschun, D. Haddad, A. Cossaro, A. Verdini, L. Floreano, T. Kluner, F. D. Toste, E. Gross, *Chem. Eur. J.* **2019**, *25*, 15067–15072; e) S. Dery, S. Kim, G. Tomaschun, I. Berg, D. Feferman, A. Cossaro, A. Verdini, L. Floreano, T. Kluner, F. D. Toste, E. Gross, *J. Phys. Chem. Lett.* **2019**, *10*, 5099–5104; f) M. J. MacLeod, A. J. Goodman, H. Z. Ye, H. V. T. Nguyen, T. Van Voorhis, J. A. Johnson, *Nat. Chem.* **2019**, *11*, 57–63; g) D. T. Nguyen, M. Freitag, C. Gutheil, K. Sotthewes, B. J. Tyler, M. Bockmann, M. Das, F. Schluter, N. L. Doltsinis, H. F. Arlinghaus, B. J. Ravoo, F. Glorius, *Angew. Chem. Int. Ed.* **2020**, *59*, 13651–13656; h) E. Amit, L. Dery, S. Dery, S. Kim, A. Roy, Q. C. Hu, V. Gutkin, H. Eisenberg, T. Stein, D. Mandler, F. D. Toste, E. Gross, *Nat. Commun.* **2020**, *11*, 5714; i) S. Dery, I. Berg, S. Kim, A. Cossaro, A. Verdini, L. Floreano, F. D. Toste, E. Gross, *Langmuir* **2020**, *36*, 697–703; j) I. Berg, L. Hale, M. Carmiel-Kostan, F. D. Toste, E. Gross, *Chem. Commun.* **2021**, *57*, 5342–5345; k) S. Dery, I. Alshanski, E. Mervinetsky, D. Feferman, S. Yitzchaik, M. Hurevich, E. Gross, *Chem. Commun.* **2021**, *57*, 6233–6236; l) S. Dery, P. Bellotti, T. Ben-Tzvi, M. Freitag, T. Shahar, A. Cossaro, A. Verdini, L. Floreano, F. Glorius, E. Gross, *Langmuir* **2021**, *37*, 10029–10035; m) P. Bellotti, M. Koy, M. N. Hopkinson, F. Glorius, *Nat. Chem. Rev.* **2021**, *5*, 711–725.

[4] a) Z. J. Li, M. R. Narouz, K. Munro, B. Hao, C. M. Crudden, J. H. Horton, H. X. Hao, *ACS Appl. Mater. Interfaces* **2017**, *9*, 39223–39234; b) S. R. Thomas, A. Casini, *J. Organomet. Chem.* **2021**, *938*, 121743.

[5] a) C. Richter, K. Schaepe, F. Glorius, B. J. Ravoo, *Chem. Commun.* **2014**, *50*, 3204–3207; b) M. J. MacLeod, J. A. Johnson, *J. Am. Chem. Soc.* **2015**, *137*, 7974–7977; c) H. P. Lu, Z. H. Zhou, O. V. Prezhdo, R. L. Brutchey, *J. Am. Chem. Soc.* **2016**, *138*, 14844–14847; d) K. Salorinne, R. W. Y. Man, C. H. Li, M. Taki, M. Nambo, C. M. Crudden, *Angew. Chem. Int. Ed.* **2017**, *56*, 6198–6202; e) L. M. Martinez-Prieto, L. Rakers, A. M. Lopez-Vinasco, I. Cano, Y. Coppel, K. Philippot, F. Glorius, B. Chaudret, P. W. N. M. van Leeuwen, *Chem. Eur. J.* **2017**, *23*, 12779–12786; f) H. P. Lu, R. L. Brutchey, *Chem. Mater.* **2017**, *29*, 1396–1403; g) M. R. Narouz, K. M. Osten, P. J. Unsworth, R. W. Y. Man, K. Salorinne, S. Takano, R. Tomihara, S. Kaappa, S. Malola, C. T. Dinh, J. D. Padmos, K. Ayoo, P. J. Garrett, M. Nambo, J. H. Horton, E. H. Sargent, H. Hakkinen, T. Tsukuda, C. M. Crudden, *Nat. Chem.* **2019**, *11*, 419–425; h) N. Kaeffer, D. Mance, C. Coperet, *Angew. Chem. Int. Ed.* **2020**, *59*, 19999–20007; i) D. E. Westmoreland, R. Lopez-Arteaga, E. A. Weiss, *J. Am. Chem. Soc.* **2020**, *142*, 2690–2696; j) H. Shen, Q. Y. Wu, S. Malola, Y. Z. Han, Z. Xu, R. X. Qin, X. K. Tang, Y. B. Chen, B. K. Teo, H. Hakkinen, N. F. Zheng, *J. Am. Chem. Soc.* **2022**, *144*, 10844–10853.

[6] a) Y. Levratovsky, E. Gross, *Faraday Discuss.* **2016**, *188*, 345–353; b) C. Y. Wu, W. J. Wolf, Y. Levartovsky, H. A. Bechtel, M. C. Martin, F. D. Toste, E. Gross, *Nature* **2017**, *541*, 511–515; c) S. Dery, E. Amit, E. Gross, *Top. Catal.* **2018**, *61*, 923–939; d) S. Dery, S. Kim, D. Haddad, A. Cossaro, A. Verdini, L. Floreano, F. D. Toste, E. Gross, *Chem. Sci.* **2018**, *9*, 6523–6531; e) S. Dery, S. Kim, D. Feferman, H. Mehlman, F. D. Toste, E. Gross, *Phys. Chem. Chem. Phys.* **2020**, *22*, 18765–18769; f) L. Rikanati, S. Dery, E. Gross, *J. Chem. Phys.* **2021**, *155*, 204704; g) S. Dery, H. Mehlman, L. Hale, M. Carmiel-Kostan, R. Yemini, T. Ben-Tzvi, M. Noked, F. D. Toste, E. Gross, *ACS Catal.* **2021**, *11*, 9875–9884.

[7] a) H. K. Kim, A. S. Hyla, P. Winget, H. Li, C. M. Wyss, A. J. Jordan, F. A. Larrain, J. P. Sadighi, C. Fuentes-Hemandez, B. Kippelen, J. L. Bredas, S. Barlow, S. R. Marder, *Chem. Mater.* **2017**, *29*, 3403–3411; b) A. F. Lv, M. Freitag, K. M. Chepiga, A. H. Schafer, F. Glorius, L. F. Chi, *Angew. Chem. Int. Ed.* **2018**, *57*, 4792–4796; c) S. Kang, S. Park, H. Kang, S. J. Cho, H. Song, H. J. Yoon, *Chem. Commun.* **2019**, *55*, 8780–8783; d) Z. F. Wang, M. Das, C. Gutheil, H. Osthues, F. Strieth-Kalthoff, A. Timmer, N. L. Doltsinis, W. C. Wang, L. F. Chi, F. Glorius, *J. Mater. Chem. C* **2022**, *10*, 8589–8595.

[8] I. Berg, E. Amit, L. Hale, F. D. Toste, E. Gross, *Angew. Chem. Int. Ed.* **2022**, *61*, e202201093.

[9] a) K. V. S. Ranganath, J. Kloesges, A. H. Schafer, F. Glorius, *Angew. Chem. Int. Ed.* **2010**, *49*, 7786–7789; b) P. Lara, A. Suarez, V. Colliere, K. Philippot, B. Chaudret, *ChemCatChem* **2014**, *6*, 87–90; c) R. Ye, A. V. Zhukhovitskiy, R. V. Kazantsev, S. C. Fakra, B. B. Wickemeyer, F. D. Toste, G. A. Somorjai, *J. Am. Chem. Soc.* **2018**, *140*, 4144–4149; d) P. Tegeder, M. Freitag, K. M. Chepiga, S. Muratsugu, N. Moller, S. Lamping, M. Tada, F. Glorius, B. J. Ravoo, *Chem. Eur. J.* **2018**, *24*, 18682–18688; e) L. Stephens, J. D. Padmos, M. R. Narouz, A. Al-Rashed, C. H. Li, N. Payne, M. Zamora, C. M. Crudden, J. Mauzeroll, J. H. Horton, *J. Electrochem. Soc.* **2018**, *165*, G139–G145; f) N. Kaeffer, H. J. Liu, H. K. Lo, A. Fedorov, C. Coperet, *Chem. Sci.* **2018**, *9*, 5366–5371; g) X. X. Gou, T. Liu, Y. Y. Wang, Y. F. Han, *Angew. Chem. Int. Ed.* **2020**, *59*, 16683–16689.

[10] a) T. Droge, F. Glorius, *Angew. Chem. Int. Ed.* **2010**, *49*, 6940–6952; b) D. J. Nelson, S. P. Nolan, *Chem. Soc. Rev.* **2013**, *42*, 6723–6753; c) H. V. Huynh, *Chem. Rev.* **2018**, *118*, 9457–9492.

[11] a) A. V. Zhukhovitskiy, M. G. Mavros, T. Van Voorhis, J. A. Johnson, *J. Am. Chem. Soc.* **2013**, *135*, 7418–7421; b) C. R. Larrea, C. J. Baddeley, M. R. Narouz, N. J. Mosey, J. H. Horton, C. M. Crudden, *ChemPhysChem* **2017**, *18*, 3536–3539; c) G. Q. Wang, A. Ruhling, S. Amirjalayer, M. Knor, J. B. Ernst, C. Richter, H. J. Gao, A. Timmer, H. Y. Gao, N. L. Doltsinis, F. Glorius, H. Fuchs, *Nat. Chem.* **2017**, *9*, 152–156; d) A. Bakker, A. Timmer, E. Kolodzeiski, M. Freitag, H. Y. Gao, H. Monig, S. Amirjalayer, F. Glorius, H. Fuchs, *J. Am. Chem. Soc.* **2018**, *140*, 11889–11892.

[12] a) V. Lavallo, Y. Canac, C. Prasang, B. Donnadieu, G. Bertrand, *Angew. Chem. Int. Ed.* **2005**, *44*, 5705–5709; b) A. Bakker, M. Freitag, E. Kolodzeiski, P. Bellotti, A. Timmer, J. D. Ren, B. S. Lammers, D. Moock, H. W. Roesky, H. Monig, S. Amirjalayer, H. Fuchs, F. Glorius, *Angew. Chem. Int. Ed.* **2020**, *59*, 13643–13646.
[13] D. T. H. Nguyen, L. R. Shultz, T. Jurca, A. Nazemi, *Langmuir* **2023**, *39*, 3204–3215.
[14] E. Amit, I. Berg, E. Gross, *Chem. Eur. J.* **2020**, *26*, 13046–13052.
[15] M. M. D. Roy, E. Rivard, *Acc. Chem. Res.* **2017**, *50*, 2017–2025.
[16] a) N. Kuhn, H. Bohnen, J. Kreutzberg, D. Blaser, R. Boese, *J. Chem. Soc. Chem. Commun.* **1993**, 1136–1137; b) M. M. Hansmann, P. W. Antoni, H. Pesch, *Angew. Chem. Int. Ed.* **2020**, *59*, 5782–5787.
[17] S. M. I. Al-Rafia, A. C. Malcolm, S. K. Liew, M. J. Ferguson, R. McDonald, E. Rivard, *Chem. Commun.* **2011**, *47*, 6987–6989.
[18] S. Naumann, *Chem. Commun.* **2019**, *55*, 11658–11670.
[19] a) A. Furstner, M. Alcarazo, R. Goddard, C. W. Lehmann, *Angew. Chem. Int. Ed.* **2008**, *47*, 3210–3214; b) B. Maji, M. Horn, H. Mayr, *Angew. Chem. Int. Ed.* **2012**, *51*, 6231–6235; c) K. Powers, C. Hering-Junghans, R. McDonald, M. J. Ferguson, E. Rivard, *Polyhedron* **2016**, *108*, 8–14.
[20] a) A. Dumrath, X. F. Wu, H. Neumann, A. Spannenberg, R. Jackstell, M. Beller, *Angew. Chem. Int. Ed.* **2010**, *49*, 8988–8992; b) Y. B. Wang, Y. M. Wang, W. Z. Zhang, X. B. Lu, *J. Am. Chem. Soc.* **2013**, *135*, 11996–12003; c) M. Blumel, R. D. Crocker, J. B. Harper, D. Enders, T. V. Nguyen, *Chem. Commun.* **2016**, *52*, 7958–7961; d) W. Y. Li, N. Yang, Y. J. Lyu, *J. Org. Chem.* **2016**, *81*, 5303–5313; e) V. B. Saptal, B. M. Bhanage, *ChemSusChem* **2016**, *9*, 1980–1985; f) U. Kaya, U. P. N. Tran, D. Enders, J. Ho, T. V. Nguyen, *Org. Lett.* **2017**, *19*, 1398–1401; g) A. Schumann, C. Hering-Junghans, *Eur. J. Inorg. Chem.* **2018**, 2584–2588; h) I. C. Watson, A. Schumann, H. Y. Yu, E. C. Davy, R. McDonald, M. J. Ferguson, C. Hering-Junghans, E. Rivard, *Chem. Eur. J.* **2019**, *25*, 9678–9690.
[21] a) S. M. I. Al-Rafia, M. J. Ferguson, E. Rivard, *Inorg. Chem.* **2011**, *50*, 10543–10545; b) Y. Z. Wang, M. Y. Abraham, R. J. Gilliard, D. R. Sexton, P. R. Wei, G. H. Robinson, *Organometallics* **2013**, *32*, 6639–6642; c) R. S. Ghadwal, S. O. Reichmann, F. Engelhardt, D. M. Andrada, G. Frenking, *Chem. Commun.* **2013**, *49*, 9440–9442; d) S. M. I. Al-Rafia, M. R. Momeni, R. McDonald, M. J. Ferguson, A. Brown, E. Rivard, *Angew. Chem. Int. Ed.* **2013**, *52*, 6390–6395; e) K. Schwedtmann, R. Schoemaker, F. Hennersdorf, A. Bauza, A. Frontera, R. Weiss, J. J. Weigand, *Dalton Trans.* **2016**, *45*, 11384–11396; f) A. Causero, H. Elsen, J. Pahl, S. Harder, *Angew. Chem. Int. Ed.* **2017**, *56*, 6906–6910; g) C. Hering-Junghans, P. Andreiuk, M. J. Ferguson, R. McDonald, E. Rivard, *Angew. Chem. Int. Ed.* **2017**, *56*, 6272–6275; h) A. P. D. Batista, A. G. S. de Oliveira-Filho, S. E. Galembeck, *ACS Omega* **2017**, *2*, 299–307; i) T. X. Gentner, G. Ballmann, J. Pahl, H. Eisen, S. Harder, *Organometallics* **2018**, *37*, 4473–4480.
[22] a) P. P. Ponti, J. C. Baldwin, W. C. Kaska, *Inorg. Chem.* **1979**, *18*, 873–875; b) M. Viciano, M. Feliz, R. Corberan, J. A. Mata, E. Clot, E. Peris, *Organometallics* **2007**, *26*, 5304–5314; c) G. Y. Song, X. W. Li, Z. C. Song, J. Zhao, H. J. Zhang, *Chem. Eur. J.* **2009**, *15*, 5535–5544; d) A. Iturmendi, N. Garcia, E. A. Jaseer, J. Munarriz, P. J. S. Miguel, V. Polo, M. Iglesias, L. A. Oro, *Dalton Trans.* **2016**, *45*, 12835–12845.
[23] a) S. Naumann, A. W. Thomas, A. P. Dove, *Angew. Chem. Int. Ed.* **2015**, *54*, 9550–9554; b) H. Y. Wang, Q. Y. Wang, J. H. He, Y. T. Zhang, *Polym. Chem.* **2019**, *10*, 3597–3603; c) P. Walther, A. Krauss, S. Naumann, *Angew. Chem. Int. Ed.* **2019**, *58*, 10737–10741.
[24] a) M. B. Gildner, T. W. Hudnall, *Chem. Commun.* **2019**, *55*, 12300–12303; b) G. R. Meng, L. Kakalis, S. P. Nolan, M. Szostak, *Tetrahedron Lett.* **2019**, *60*, 378–381; c) L. M. Sherman, S. L. Strausser, R. K. Borsari, D. M. Jenkins, J. P. Camden, *Langmuir* **2021**, *37*, 5864–5871.
[25] a) M. J. Trujillo, S. L. Strausser, J. C. Becca, J. F. DeJesus, L. Jensen, D. M. Jenkins, J. P. Camden, *J. Phys. Chem. Lett.* **2018**, *9*, 6779–6785; b) J. F. DeJesus, M. J. Trujillo, J. P. Camden, D. M. Jenkins, *J. Am. Chem. Soc.* **2018**, *140*, 1247–1250; c) G. Lovat, E. A. Doud, D. Y. Lu, G. Kladnik, M. S. Inkpen, M. L. Steigerwald, D. Cvetko, M. S. Hybertsen, A. Morgante, X. Roy, L. Venkataraman, *Chem. Sci.* **2019**, *10*, 930–935.
[26] a) L. Floreano, A. Cossaro, R. Gotter, A. Verdini, G. Bavdek, F. Evangelista, A. Ruocco, A. Morgante, D. Cvetko, *J. Phys. Chem. C* **2008**, *112*, 10794–10802; b) A. Calabrese, L. Floreano, A. Verdini, C. Mariani, M. G. Betti, *Phys. Rev. B* **2009**, *79*, 115446.
[27] M. R. Narouz, C. H. Li, A. Nazemi, C. M. Crudden, *Langmuir* **2017**, *33*, 14211–14219.
[28] X. P. Cao, R. J. Hamers, *J. Am. Chem. Soc.* **2001**, *123*, 10988–10996.
[29] N. Graf, E. Yegen, T. Gross, A. Lippitz, W. Weigel, S. Krakert, A. Terfort, W. E. S. Unger, *Surf. Sci.* **2009**, *603*, 2849–2860.
[30] a) S. Rangan, F. Bournel, J. J. Gallet, S. Kubsky, K. Le Guen, G. Dufour, F. Rochet, F. Sirotti, S. Carniato, V. Ilakovac, *Phys. Rev. B* **2005**, *71*, 165319; b) V. Ilakovac, S. Carniato, J. J. Gallet, E. Kukk, D. Horvatic, A. Ilakovac, *Phys. Rev. A* **2008**, *77*, 012516; c) H. Min, P. L. Girard-Lauriault, T. Gross, A. Lippitz, P. Dietrich, W. E. S. Unger, *Anal. Bioanal. Chem.* **2012**, *403*, 613–623.
[31] Y. H. La, Y. J. Jung, T. H. Kang, K. Ihm, K. J. Kim, B. Kim, J. W. Park, *Langmuir* **2003**, *19*, 9984–9987.
[32] M. Jain, U. Gerstmann, W. G. Schmidt, H. Aldahhak, *J. Comput. Chem.* **2022**, *43*, 413–420.
[33] A. Ravikumar, A. Baby, H. Lin, G. P. Brivio, G. Fratesi, *Sci. Rep.* **2016**, *6*, 24603.
[34] R. J. J. Jansen, H. Vanbekkum, *Carbon* **1995**, *33*, 1021–1027.

Manuscript received: August 14, 2023
Accepted manuscript online: September 24, 2023
Version of record online: October 11, 2023

Angewandte Chemie
Eine Zeitschrift der Gesellschaft Deutscher Chemiker

Supporting Information

Self-Assembled Monolayers of N-Heterocyclic Olefins on Au(111)

*I. Berg, L. Schio, J. Reitz, E. Molteni, L. Lahav, C. G. Bolaños, A. Goldoni, C. Grazioli, G. Fratesi, M. M. Hansmann, L. Floreano, E. Gross**

Table of contents

Synthesis of NHO

Materials and Methods

All solvents were purified by distillation over the drying agents indicated, or stored over molecular sieves and degassed with argon. NMR spectra were measured on the following spectrometers Bruker AV 500 Avance NEO, Bruker AV 400 Avance III HD NanoBay, AV 600 Avance III HD and AV 700 Avance III HD and chemical shifts (δ) are referenced to their solvent signals [C_6D_6, 7.16 (^{1}H NMR) 128.06 (^{13}C NMR); CD_3CN, 1.94 (^{1}H NMR) 118.26 (^{13}C NMR), $CDCl_3$ 7.26 (^{1}H NMR) 77.16 (^{13}C NMR), CD_2Cl_2, 5.32 (^{1}H NMR) 54.00 (^{13}C NMR), d_8-thf, 3.58 (^{1}H NMR) 67.57 (^{13}C NMR)], coupling constants (*J*) in Hz. All spectra were recorded in 5 mm NMR tubes at the temperatures indicated. The solvent signals were used as references and the chemical shifts converted to the TMS scale. All commercially available compounds (Acros, ABCR, Alfa Aesar, Sigma Aldrich, Fluorochem) were used as received. IR-ATR measurements (diamond) were performed in reflection mode on a Bruker Alpha II inside a glovebox, wavenumbers in cm^{-1}. Amberlyst A-26(OH) was purchased from Sigma-Aldrich and used as obtained.

Synthesis of NHO-1H I^-

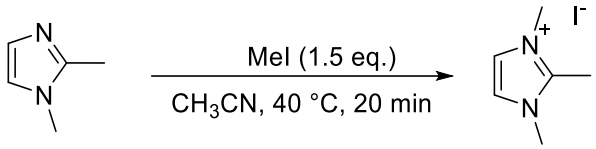

NHO-1H I^- was prepared according to the literature procedure.[1]

Under an atmosphere of argon 1,2-dimethylimidazole (2.00 g, 20.8 mmol, 1.0 eq.) is dissolved in acetonitrile (10 mL). Iodomethane is added (1.94 mL, 31.2 mmol, 1.5 eq.) and the solution is stirred at 40 °C for 25 min. Et_2O (10 mL) is added and the dispersion sonicated. The precipitate is filtered off, washed with Et_2O (2 x 5 mL) and dried under reduced pressure to afford NHO-1H I^- (4.68 g, 19.7 mmol, 95%) as a colorless powder.

^{1}H NMR (400 MHz, D_2O, 298 K) δ [ppm] = 7.31 (s, 2 H), 3.79 (s, 6 H), 2.60 (s, 3 H); **^{13}C NMR** (101 MHz, D_2O, 298 K) δ [ppm] = 144.7, 121.8, 34.7, 8.9.

The NMR data is in agreement with literature reference.[1]

Synthesis of NHO-1H

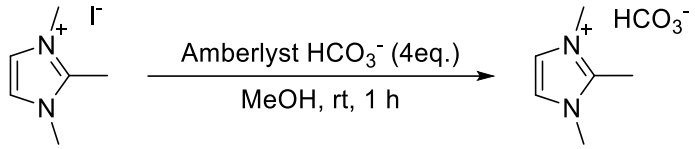

NHO-1H was prepared according to an adapted literature procedure.[2]

Amberlyst A-26(OH) (4.00 g, 4.0 eq.) is suspended in H_2O (10 mL). Under thorough stirring, CO_2 is bubbled through the suspension for 1.5 h. The Amberlyst is then filtered off and washed with MeOH (2 x 5 mL). NHO-1H I^- (1.00 g, 4.20 mmol, 1.0 eq.) dissolved in MeOH (10 mL) is added to the Amberlyst and the suspension is stirred under bubbling with CO_2 for 1 h. The beads are filtered off, rinsed with MeOH (2 x 5 mL) and the filtrate is concentrated. The residue is triturated with acetone (20 mL) and the resulting white precipitate filtered off. The precipitate is washed with acetone (2 x 5 mL) and dried under reduced pressure to afford NHO-1H (0.63 g, 3.66 mmol, 88%) as a colorless solid.

^{1}H NMR (500 MHz, D_2O, 298 K) δ [ppm] = 7.28 (s, 2H), 3.76 (s, 6H), 2.55 (s, 3H); **^{13}C NMR** (126 MHz, D_2O, 298 K) δ [ppm] = 161.0, 144.7, 121.7, 34.5, 8.6; **IR** [cm^{-1}]: 3116, 3052, 2935, 1625, 1608, 1550, 1464, 1420, 1379, 1342, 1264, 1130, 1046, 990, 838, 827, 761, 735, 687, 655, 641, 481.

The NMR data is in agreement with literature reference.[3]

Synthesis of NHO-2H I^-

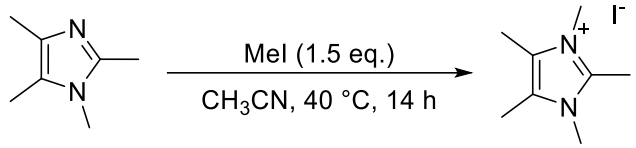

NHO-2H I^- was prepared according to the literature procedure.[4]

Under an atmosphere of argon 1,2,4,5-tetramethylimidazole (2.00 g, 16.1 mmol, 1.0 eq.) is dissolved in acetonitrile (10 mL). Iodomethane is added (1.50 mL, 24.2 mmol, 1.5 eq.) and the solution is stirred at 40 °C for 18 h. The reaction mixture is poured into Et_2O (80 mL) under vigorous stirring. The resulting precipitate is filtered off, washed with Et_2O (2 x 20 mL) and dried under reduced pressure to afford NHO-2H I^- (3.96 g, 14.9 mmol, 93%) as a colorless solid.

^{1}H NMR (400 MHz, D_2O, 298 K) δ [ppm] = 3.65-3.62 (m, 6 H), 2.59-2.57 (m, 3 H), 2.25-2.22 (m, 6 H); **^{13}C NMR** (100 MHz, D_2O, 298 K) δ [ppm] = 142.2, 125.4, 31.6, 9.8, 7.9.

The NMR data is in agreement with literature reference. [4]

Synthesis of NHO-2H

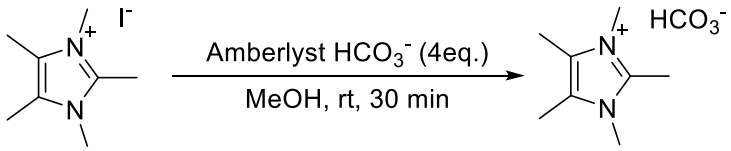

NHO-2H was prepared according to an adapted literature procedure.[2]

Amberlyst A-26(OH) (3.60 g, 4.0 eq.) is suspended in H_2O (10 mL). Under thorough stirring, CO_2 is bubbled through the suspension for 45 min. The Amberlyst is then filtered off and washed with MeOH (2 x 5 mL). I^-NHO-2 (1.00 g, 3.76 mmol, 1.0 eq.) dissolved in MeOH (10 mL) is added to the Amberlyst and the suspension is stirred under bubbling with CO_2 for 1 h. The beads are filtered off, rinsed with MeOH (2 x 5 mL) and the filtrate is concentrated. The residue is triturated with acetone (20 mL) and the resulting white precipitate filtered off. The precipitate is washed with Et_2O (2 x 5 mL) and dried under reduced pressure to afford NHO-2H. (0.62 g, 3.12 mmol, 83%) as a colorless solid.

m.p. 144 °C decomposition; **^{1}H NMR** (500 MHz, D_2O, 298 K) δ [ppm] = 3.60 (s, 6 H, NCH_3), 2.53 (s, 3 H, 2-CH_3), 2.20 (s, 6 H, 4,5-CH_3); **^{13}C NMR** (126 MHz, D_2O, 298 K) δ [ppm] = 160.2 (HCO_3^-), 142.2 (2-C_q), 125.3 (4,5-C_q), 31.2 (NCH_3), 9.2 (2-CH_3), 7.6 (4,5-CH_3); **IR** [cm^{-1}]: 2928, 1672, 1639, 1542, 1446, 1423, 1407, 1382, 1357, 1323, 1235, 1140, 1075, 1046, 973, 835, 680, 641, 580, 563.

Deposition, Spectroscopic Characterization and DFT Calculations

Au (111) single crystal with a diameter of 10 mm (purchased from SPL) was cleaned under ultrahigh vacuum conditions by three consecutive cycles of sputtering (2×10^{-6} torr Ar; 1.5 keV; 20 min) and subsequent annealing to 500 °C (two thermocouples in direct contact with the sample). The effectiveness of the cleaning procedure was validated by monitoring the C1s XPS signal (Figure S27). Dimethylimidazolium-2-carboxylate was purchased from Sigma Aldrich and used as obtained.

Vapor-deposition of NHO-1**,** NHO-2 and ^{Me}NHC was performed in a UHV chamber at ALOISA beamline. The molecules were housed in a home-made Knudsen cell (boron nitride crucible with thermocouple inside). The evaporation temperature was raised to 350 K and the molecules were dosed into the UHV chamber, inducing an increase in the back-pressure in the range of 10^{-7}-10^{-8} torr. The Au surface was kept at room temperature (RT) and exposed to the evaporated molecules for 15 minutes. Several consecutive deposition cycles were conducted and N1s and C1s XPS measurements were performed after each cycle. These measurements did not show noticeable changes in the signal amplitude, thus validating the exclusive formation of a saturated monolayer on the surface.

Synchrotron radiation XPS measurements were measured with the sample at grazing incidence (α = 4.0˚) in close to p-polarization. The spectra, taken with photon energy of 515 eV (overall energy resolution of 160 meV), were measured in close to normal emission (90°-α) by a hemispherical electron analyzer with an angular acceptance angle of 2°. The binding energy (BE) was calibrated by setting the BE position of Au 4f7/2 peak to 84.0 eV. All spectra were corrected by subtracting a Shirley-type background. Analysis of the XPS peaks and their fitting was performed using CasaXPS software. Work function measurements were conducted using synchrotron radiation XPS, using low photon energies (150 eV). Bias voltage of -30.00 V was applied on the sample. The binding energy of the secondary electrons cut-off was calibrated by setting the BE position of Au 4f7/2 peak to 84.0 eV.

X-ray absorption spectra measurements were taken in partial electron yield using a channeltron detector equipped with a front grid biased at negative voltage (250 V and -370 V for the C and N *K*-edge spectra, respectively) to filter out the low energy secondary electrons. The NEXAFS spectra at the nitrogen and carbon K-edge were measured with the resolution set to ~80 meV while keeping the sample at a constant grazing angle of 6°. The orientation of the surface with respect to the photon beam polarization was changed from s-polarization to close to p-polarization by rotating the

sample coaxially to the photon beam axis. NEXAFS spectra were reported in the form of a normalized absorption amplitude ($I_{(E)} = I/I_{(reference)}$), using NEXAFS measured on Au (111) as a reference ($I_{(reference)}$). Tilt angle (θ), relative to the surface plane, was calculated based on the following formula: $\tan(\theta) = \sqrt{\frac{2I_s}{I_p}}$ in which I_s and I_p represent the s-polarized and p-polarized signal amplitudes, respectively.[5] We observed a very small residual intensity of the main π* resonance at the N K-edge in s-polarization for NHO-1, NHO-2 (Fig. 2), as well as ^{Me}NHC (Fig. S14) molecules, which indicates a practically flat adsorption geometry (tilt < 10˚) of molecules as deposited at RT. The analysis of the C K-edge NEXAFS (Fig. S15) yields a dichroism practically equivalent to that at the N K-edge for NHO-2 and ^{Me}NHC, while we observed a larger residual intensity of π* resonances in s-polarization for NHO-1, as deposited at RT, which would yield a tilt angle of ~21˚ (much larger than the 5-8˚ value drawn from N K-edge). However, the flat lying geometry of NHO-1 is recovered after a mild annealing at 150˚C, which points to a contribution of volatile carbon contaminants in the C K-edge NEXAFS spectra of NHO-1 at RT, rather than to an effective larger tilt angle.

Scanning tunneling microscopy (STM) measurements were performed at the CNR-IOM/Elettra joint laboratory for microscopy (OSMOS) in Trieste with an Aahrus type microscope (model 150 by SPECS) under Ultra-High Vacuum (UHV). The topographic images were collected by operating the STM either at room temperature (RT) or at 130 K with a tungsten tip and positive sample bias.

The STM experiments have been performed on a Au (111) single crystal (diameter 8 mm) purchased from SPL. The sample was cleaned and ordered by repeated cycles of sputtering (1.5–2 kV Ar^+ ions) and annealing up to 723 K. The sample temperature was measured with K-type thermocouples in direct contact with the sample, thus providing an accuracy better than 10 °C. Molecules were sublimated from homemade boron nitride crucibles (identical to those used at the ALOISA beamline) in an UHV preparation chamber next to the STM chamber. Both NHO-1H and NHO-2H molecules were sublimated at 350 K, with the sample kept at room temperature, obtaining a coverage close to one monolayer.

For base-induced deposition, gold films (100 nm thickness) were prepared by gold evaporation on a highly doped n-type Si wafer coated with a 10 nm thick Cr film. The samples were cleaned via a few sonication cycles in triply distilled water (TDW), acetone and isopropanol. 1,2,3 trimethyl imidazolium iodide and 1,2,3,4,5-pentamethyl imidazolium iodide precursors were dissolved in THF (30 mM) in a glove box and mixed with a THF solution of potassium tert-butoxide (60 mM) for 2 hours for deprotonation

and formation of the corresponding free carbenes. The freshly prepared solution with the activated NHOs was transferred through a syringe with filter unit to a vial in which the Au-coated Si wafers were contained. After 18 hours, the samples were removed from the glove box and rinsed three times with tetrahydrofuran, three times with distilled water and two times with ethanol. The samples were then flushed with N_2 for 5 minutes.

For liquid deposition of 1,2,3,4,5-pentamethyl imidazolium hydrogen carbonate precursor, gold films (100 nm thickness) were prepared by gold evaporation on highly doped n-type Si wafer coated with a 10 nm thick Cr film. The samples were cleaned via a few sonication cycles in triply distilled water (TDW), acetone and isopropanol. 1,2,3,4,5-pentamethyl imidazolium hydrogen carbonate precursor was dissolved in THF (30 mM) in a glove box and the gold surface was immersed in the solution. The sample was heated to 70 °C in a high-pressure glass tube for 4 hours, then rinsed three times with tetrahydrofuran, three times with distilled water and two times with ethanol, following by drying with N_2 for 5 minutes. The sample was later annealed to 150 °C for 1h under N_2.

Ab-initio calculations were performed within Density Functional Theory (DFT), as implemented in the Quantum ESPRESSO distribution [6,7] with plane waves and ultrasoft pseudopotentials.[8] We used the PBE exchange-correlation functional,[9] and we took into account van der Waals interactions by the Grimme D3 approach.[10]

The substrate was modeled by a slab approach, including 4 Au (111) layers; a 5x5 surface cell was used in the case of single molecule adsorption, a 8x5 one for dimers and a 8x8 one for trimers and tetramers. For these three surface unit cells, we sampled the Brillouin zone by a 3x3, 2x3, and 2x2 shifted Monkhorst-Pack grid, respectively.

Kinetic energy cutoffs were set to 40 Ry for the plane-wave expansion and 200 Ry for the effective potential and charge density, as standard for GBRV pseudopotentials.[8]

The molecules and adatoms were placed on one side of the slab and performed geometry optimization including two Au layers.

Tables S1-S2

Table S1. E_{ads}: adsorption energies for NHO or NHC on Au (111) or Au (111) covered by Au adatoms. Where present, the angle is the molecular azimuthal angle φ (see Figure S17). E_{form}: formation energy from gas phase molecules and bulk Au atoms. $E_{assembly}$: formation energy from individual NHO-Au complexes on surface and Au adatoms. All values in eV.

	E_{ads}/molecule	E_{form}/molecule	$E_{assembly}$/molecule
NHO-2 on bare Au(111)			
NHO-2 top 0°	-2.307		
NHO-2 top 30°	-2.280		
NHO-2 bridge 0°	-1.819		
NHO-2 bridge 30°	unstable		
NHO-2 bridge 60°	unstable		
NHO-2 bridge 90°	unstable		
NHO-2 fcc 0°	-1.761		
NHO-2 fcc 30°	-1.783		
NHO-2 fcc 60°	-1.795		
NHO-2 fcc 90°	-1.769		
NHO-2 on Au adatom			
NHO-2 (standing) / Au	-2.188	-1.398	
NHO-2 0° / Au	-2.995	-2.205	
NHO-2 30° / Au	-2.997	-2.207	
NHO-2 60° / Au	-2.983	-2.193	
NHO-2 90° / Au	-2.997	-2.206	
NHO-2-Au complexes			
2x NHO-2 / 1x Au	-2.542	-2.147	0.454
2x NHO-2 / 2x Au (dimer)	-2.933	-2.274	-0.067
3x NHO-2 / 3x Au (trimer)	-2.845	-2.290	-0.084
4x NHO-2 / 4x Au (tetramer)	-2.771	-2.283	-0.077
(2xNHO2 / 2x Au) x2 (dimer pair)	-2.716	-2.228	-0.022
NHO-1 on bare Au(111) and Au adatom			
NHO-1 top 0°	-1.963		
NHO-1 90° / Au	-2.729	-1.939	
NHO-1-Au complexes			
2x NHO-1 / 1x Au	-2.290	-1.896	0.439
2x NHO-1 / 2x Au	-2.673	-2.014	-0.074
2x NHO-1 / 3x Au	-2.653	-1.783	-0.239
NHC on bare Au(111) and Au adatom			
NHC standing	-1.861		
NHC standing / 1x Au	-2.676	-1.886	
NHC 0° / 1x Au	-2.681	-1.891	
NHC 30° / 1x Au	-2.721	-1.931	

Table S2. Calculated bond lengths and angles of NHO-1 and NHO-2. For more details regarding the annotation of the atoms and angles, see Fig. S17.

	NHO-1 free	NHO-1 on surface	NHO-1 on adatom	NHO-2 free	NHO-2 on surface	NHO-2 on adatom
C6-C1 (Å)	1.364	1.437	1.444	1.365	1.437	1.447
C6-Au (Å)		2.238	2.135		2.234	2.124
C1-N2 (Å)	1.393	1.367	1.363	1.390	1.363	1.360
Angle (C1-C6-Au) (°)		109.4	106.8		110.0	110.1
Angle (z-C6-Au) (°)		0.9	27.8		0.3	28.5
Angle (xy-C6-C1) (°)		18.5	-11.1		19.7	-8.4

Figures S1-S29

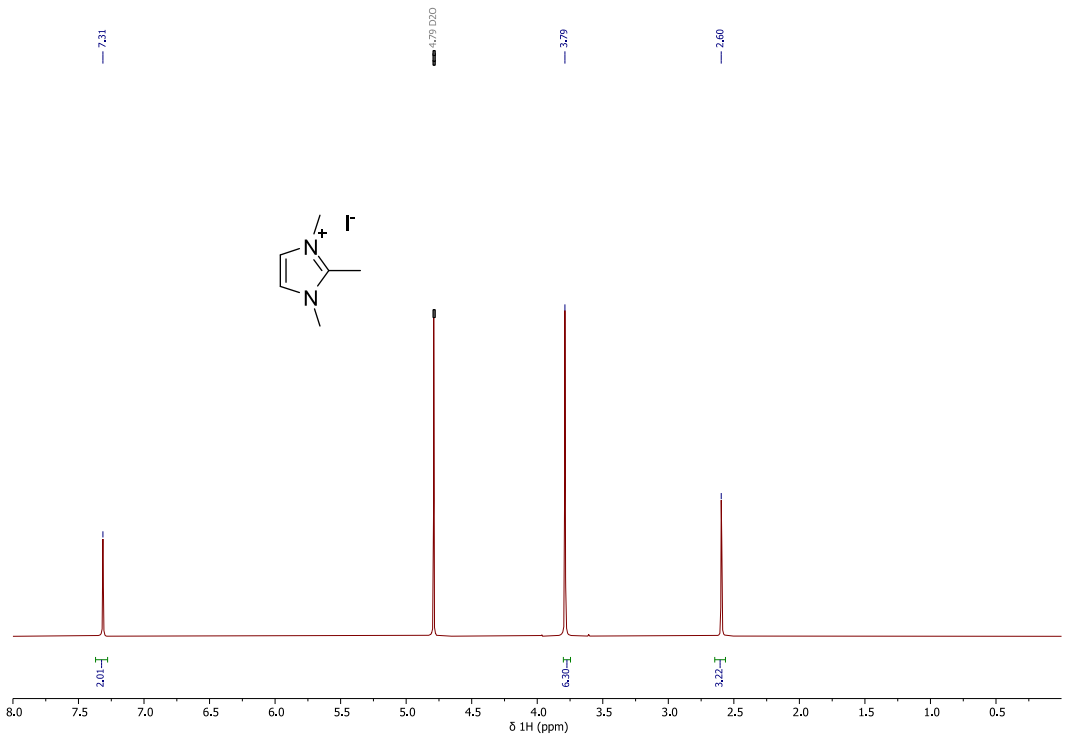

Figure S1. ^{1}H NMR (400 MHz, D_2O, 298 K) of NHO-1H I^-.

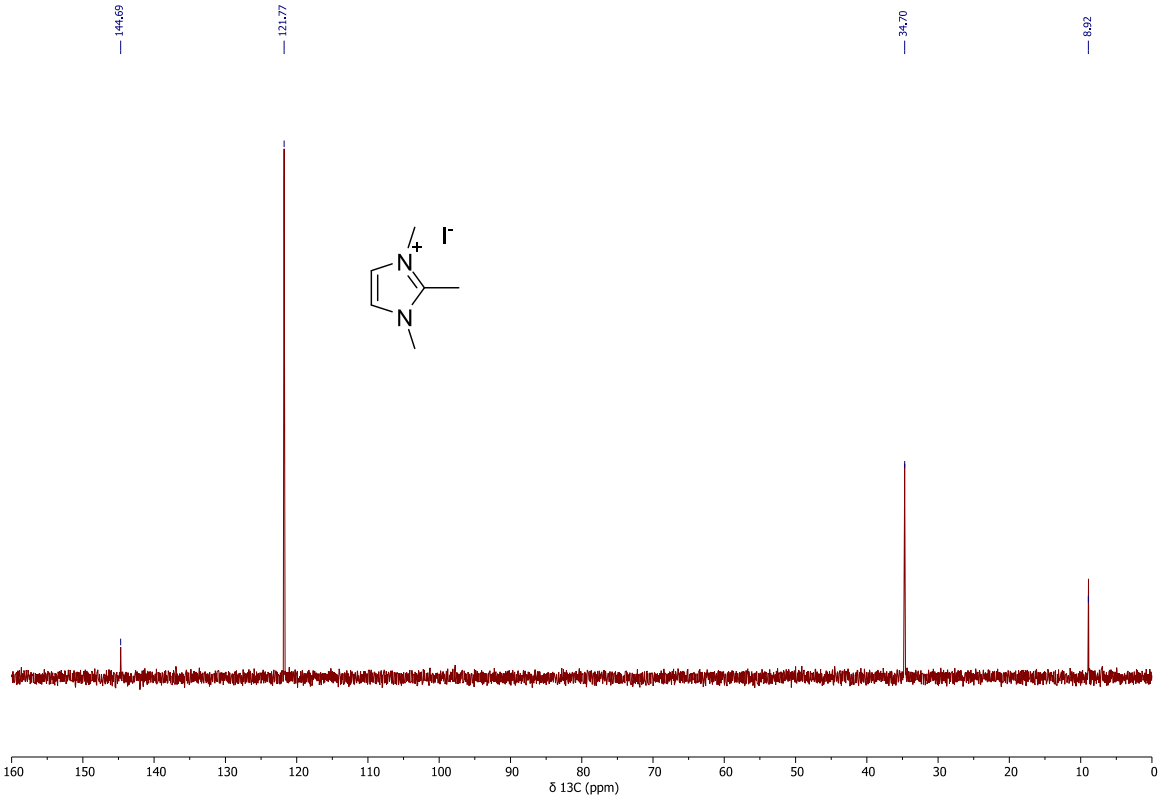

Figure S2. ^{13}C NMR (101 MHz, D_2O, 298 K) of NHO-1H I^-.

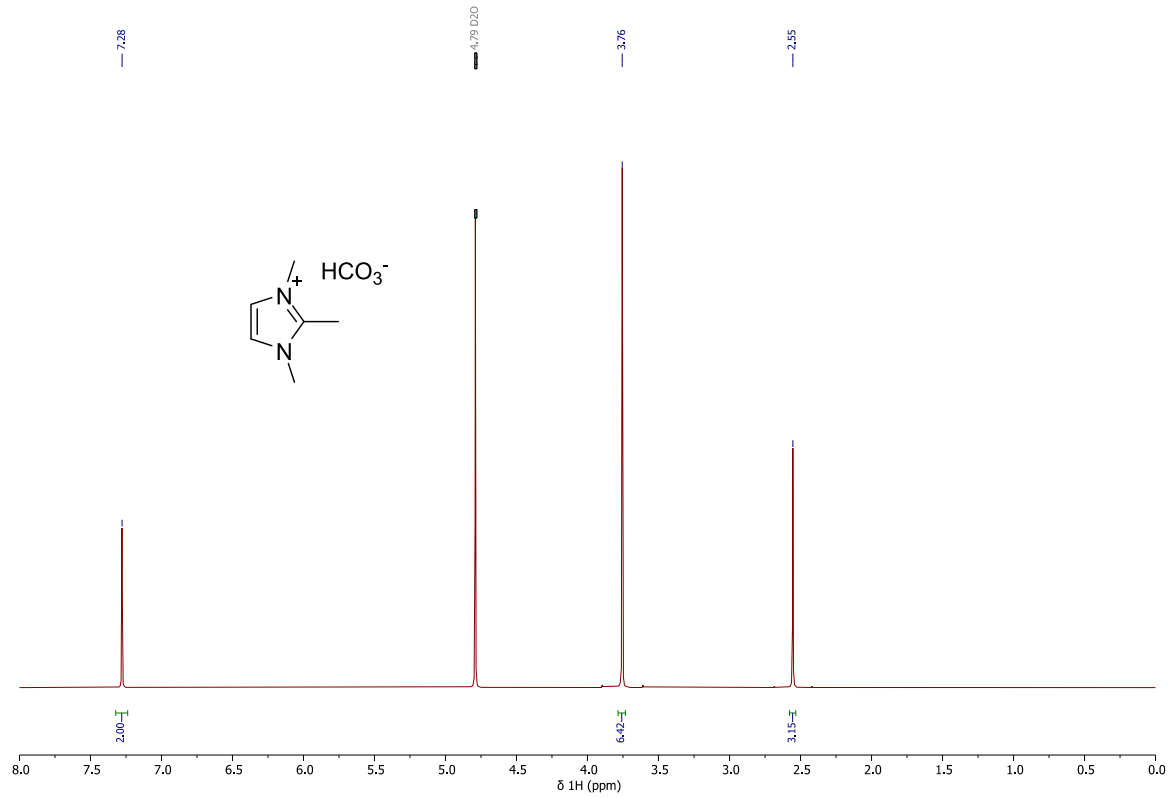

Figure S3. ^{1}H NMR (500 MHz, D_2O, 298 K) of NHO-1H precursor.

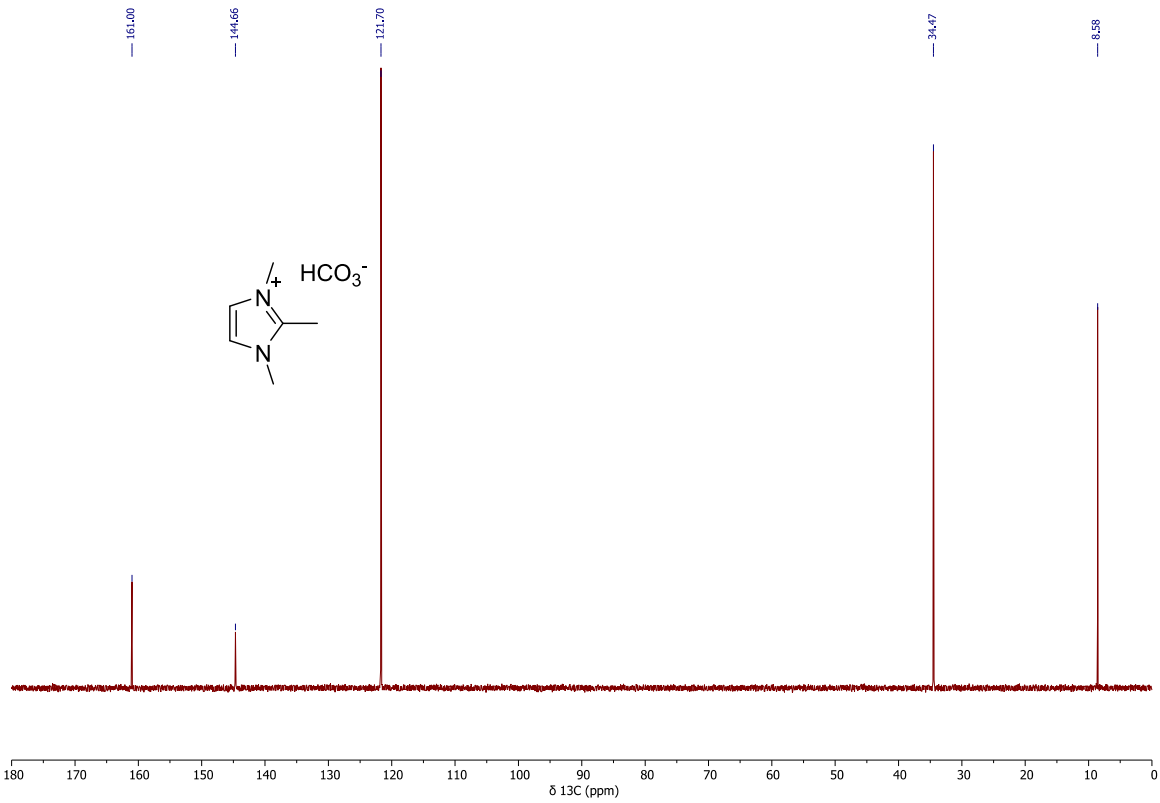

Figure S4. ^{13}C NMR (500 MHz, D_2O, 298 K) of NHO-1H precursor.

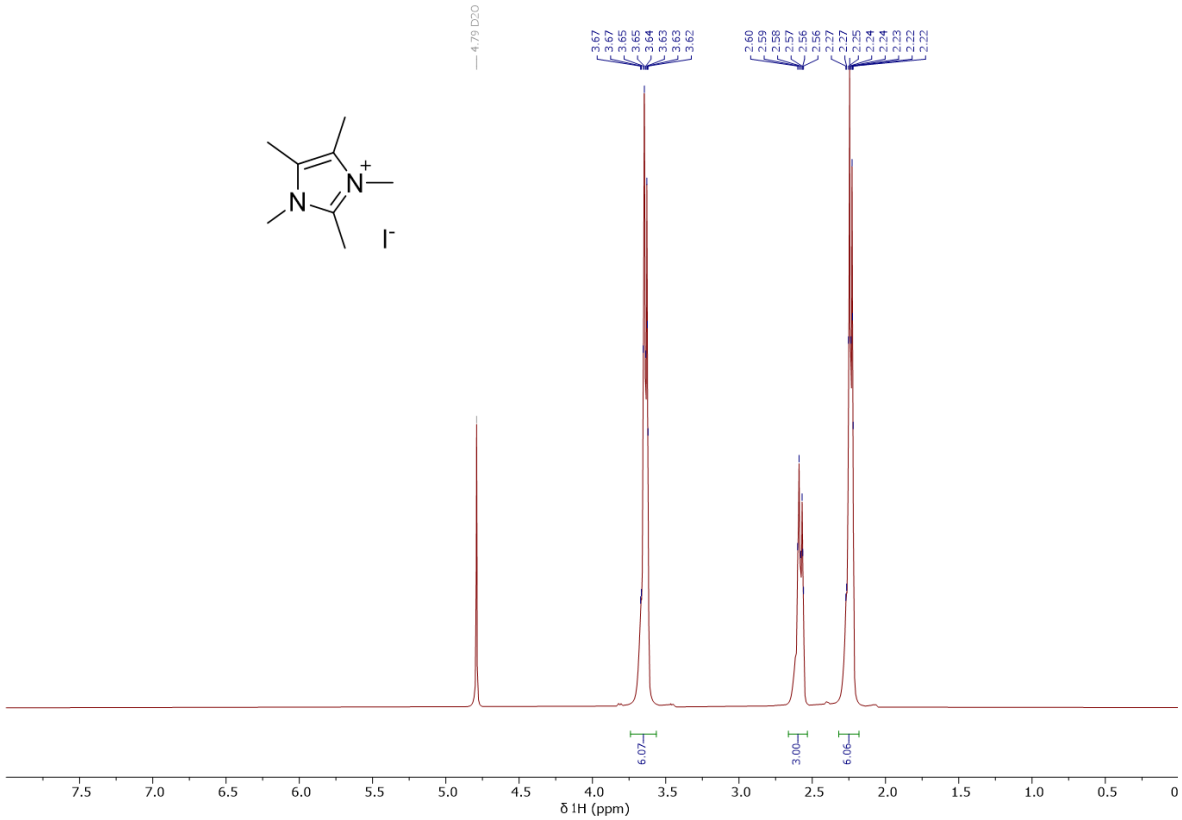

Figure S5. ^{1}H NMR (400 MHz, D_2O, 298K) of NHO-2H I^- precursor.

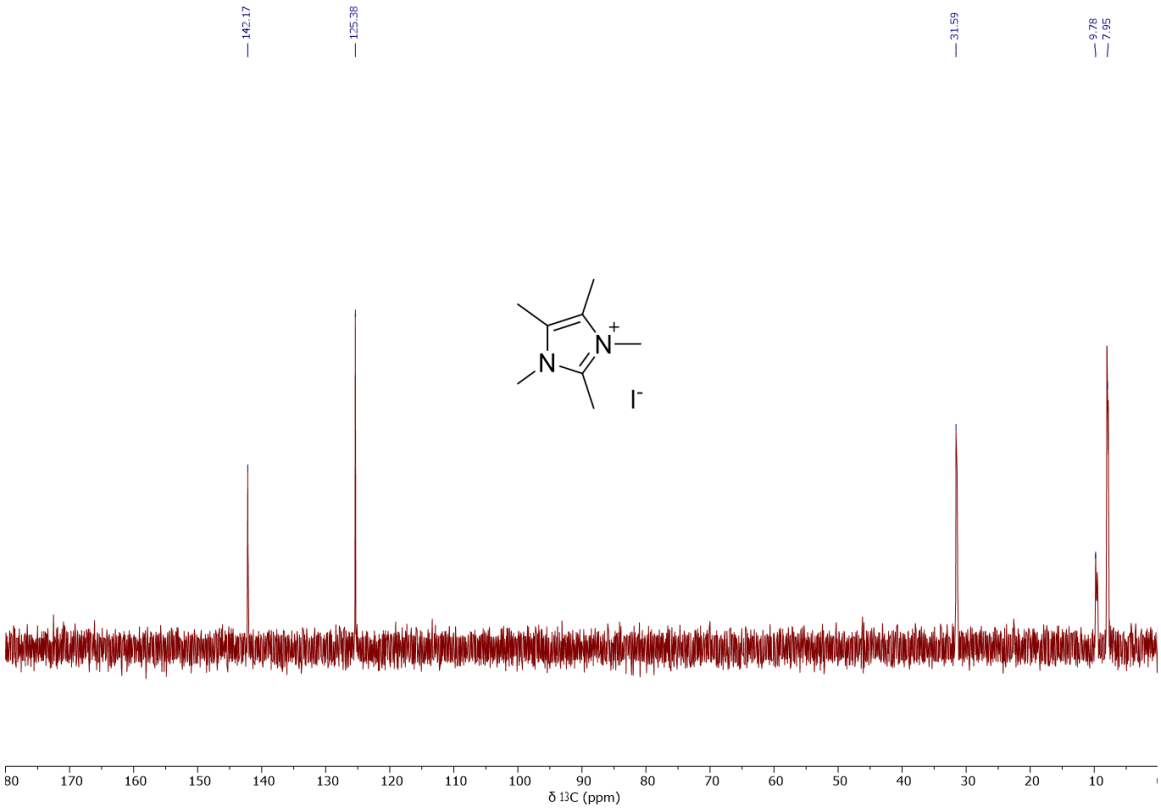

Figure S6. ^{13}C NMR (100 MHz, D_2O, 298K) of NHO-2H I^- precursor.

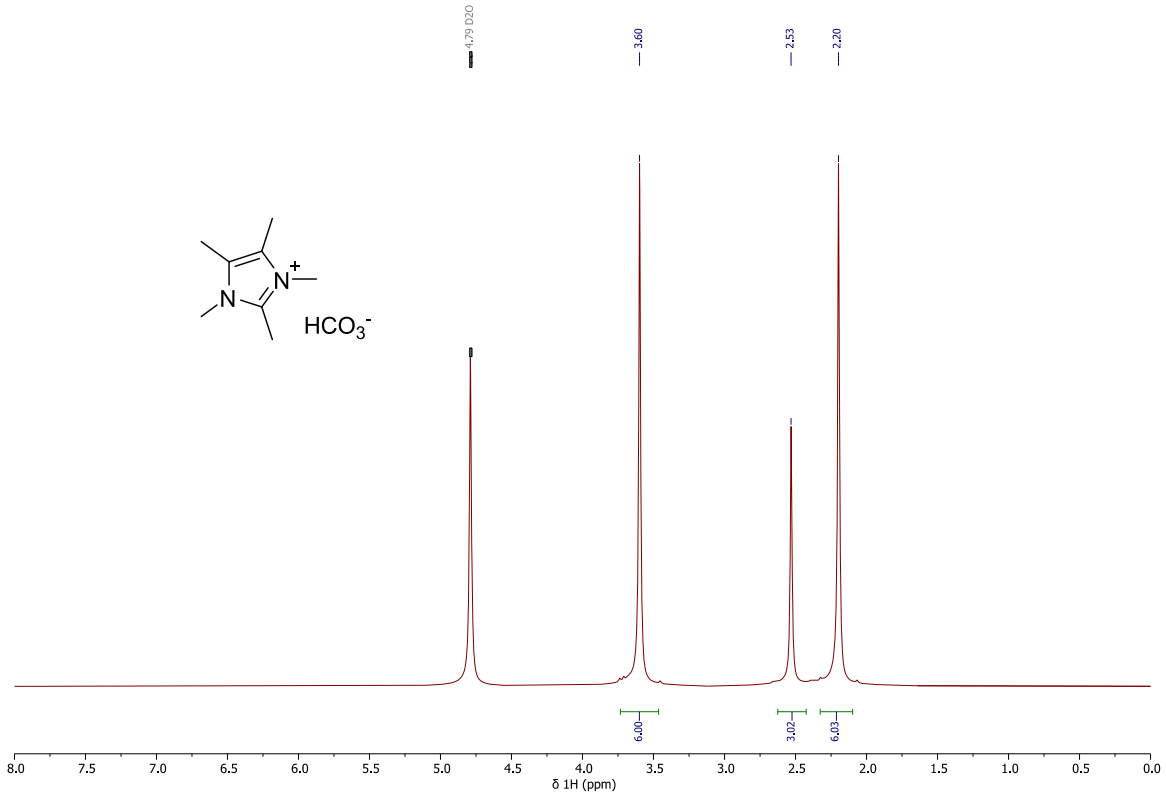

Figure S7. ^{1}H NMR (500 MHz, D_2O, 298 K) of NHO-2H precursor.

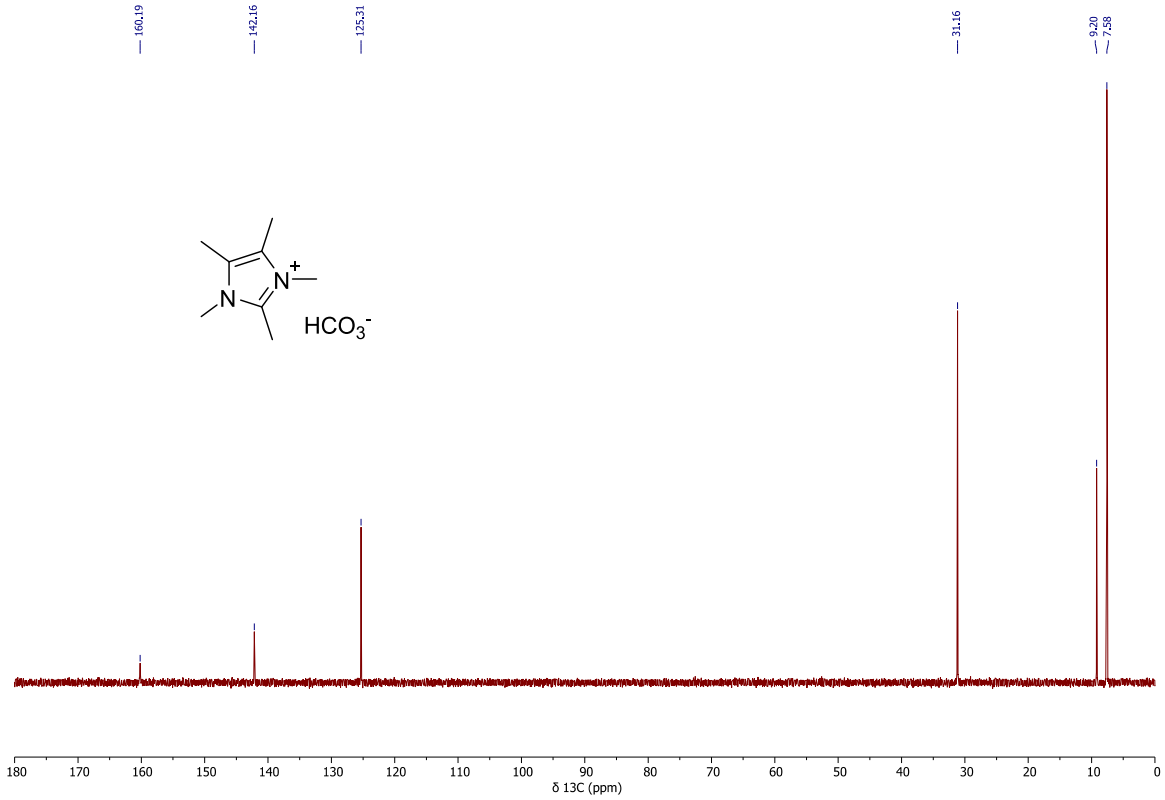

Figure S8. ^{13}C NMR (126 MHz, D_2O, 298 K) of NHO-2H precursor.

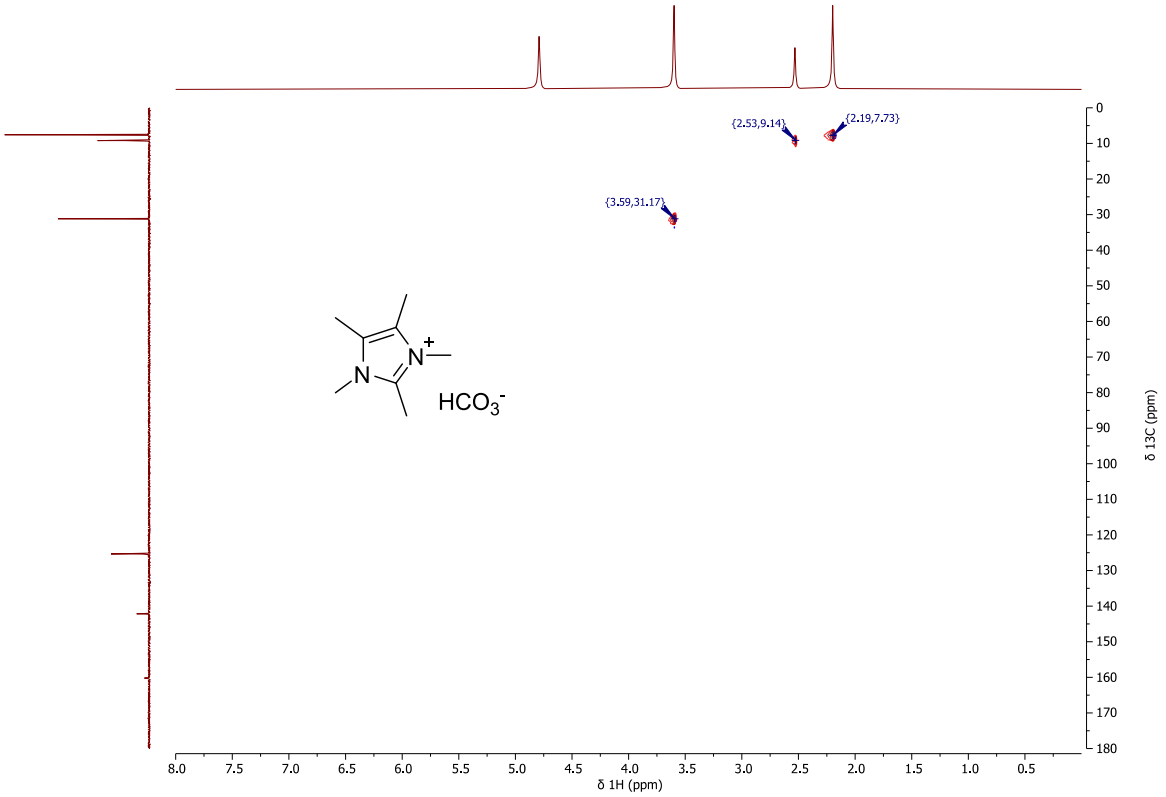

Figure S9. $^{1}H/^{13}C$ HSQC (500/125 MHz, D_2O, 298 K) of NHO-2H precursor.

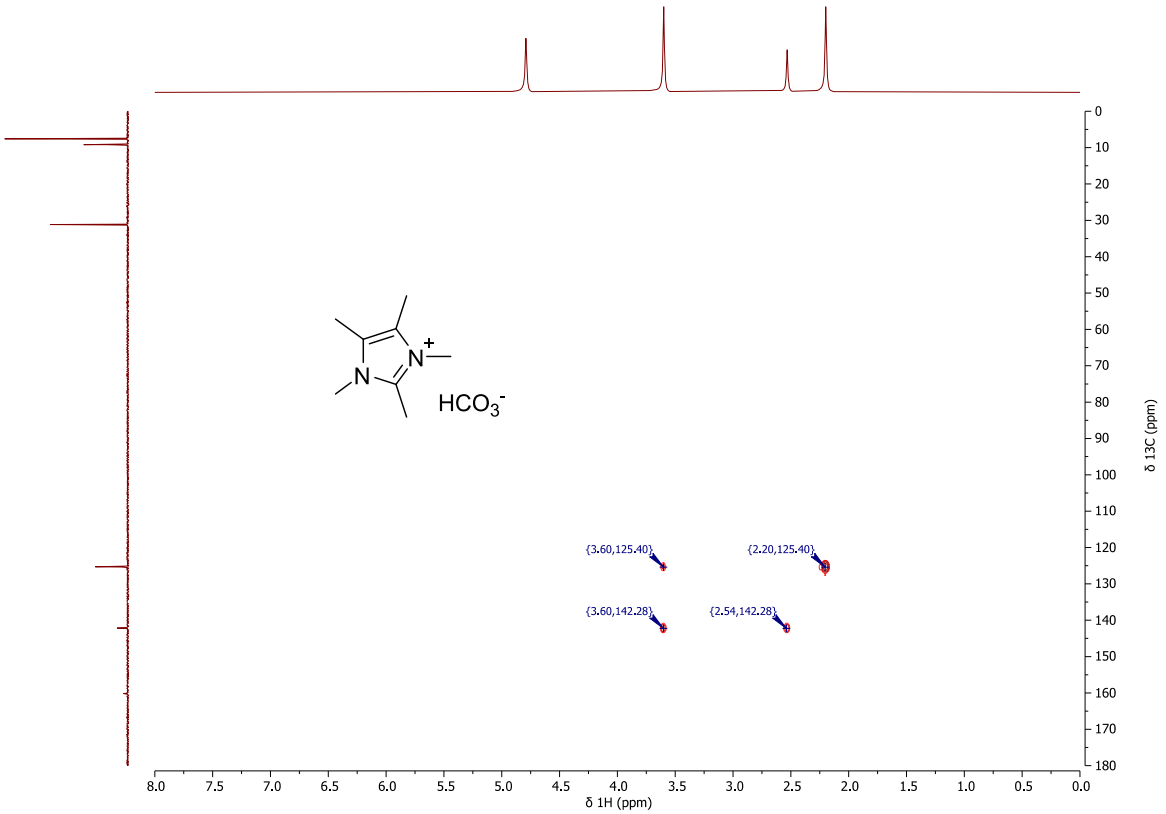

Figure S10. $^{1}H/^{13}C$ **HMBC** (500/125 MHz, D_2O, 298 K) of NHO-2H precursor.

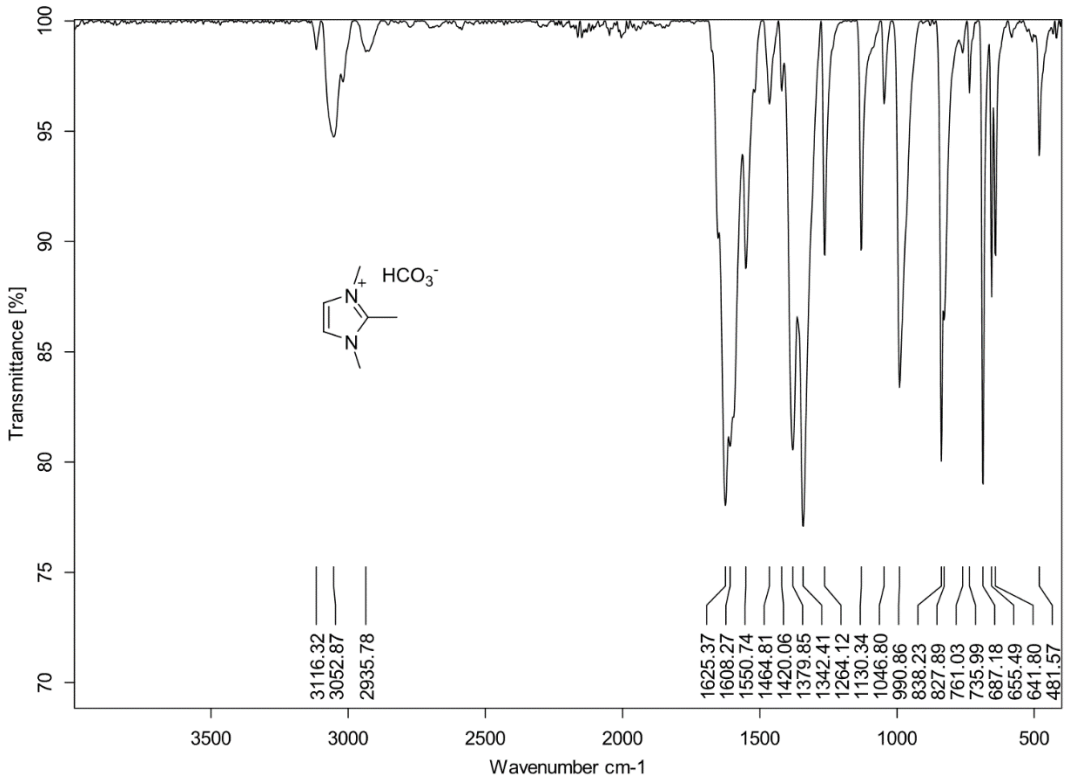

Figure S11. IR (ATR) spectrum of NHO-1H precursor.

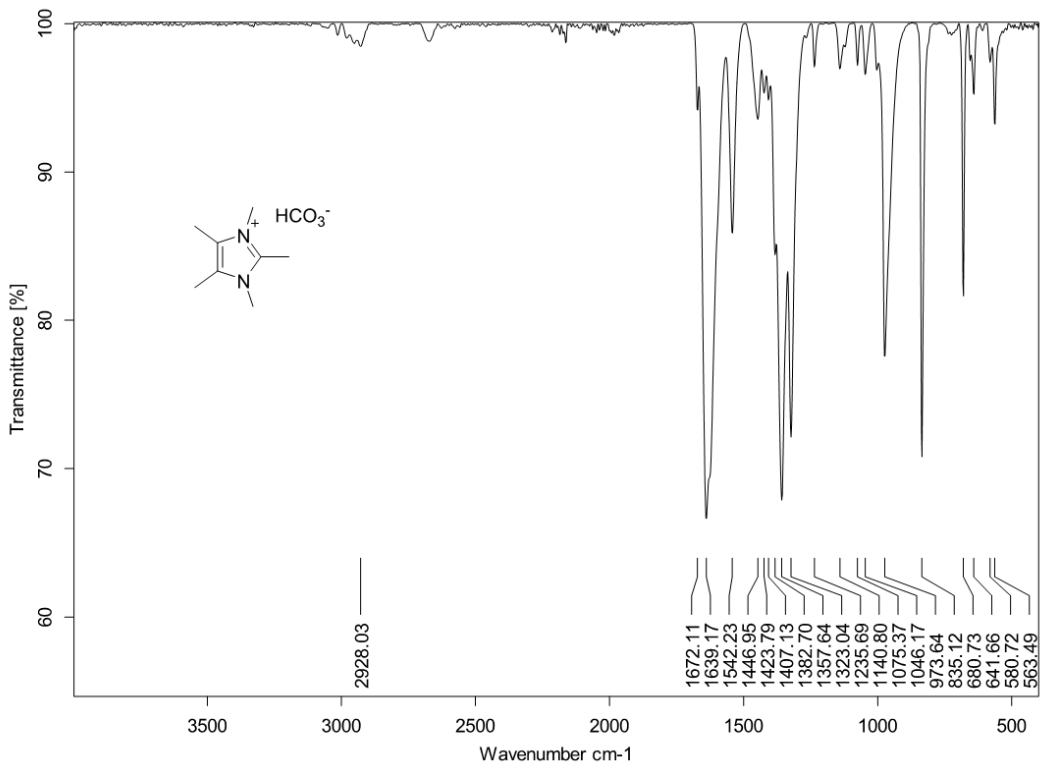

Figure S12. IR (ATR) spectrum of NHO-2H precursor.

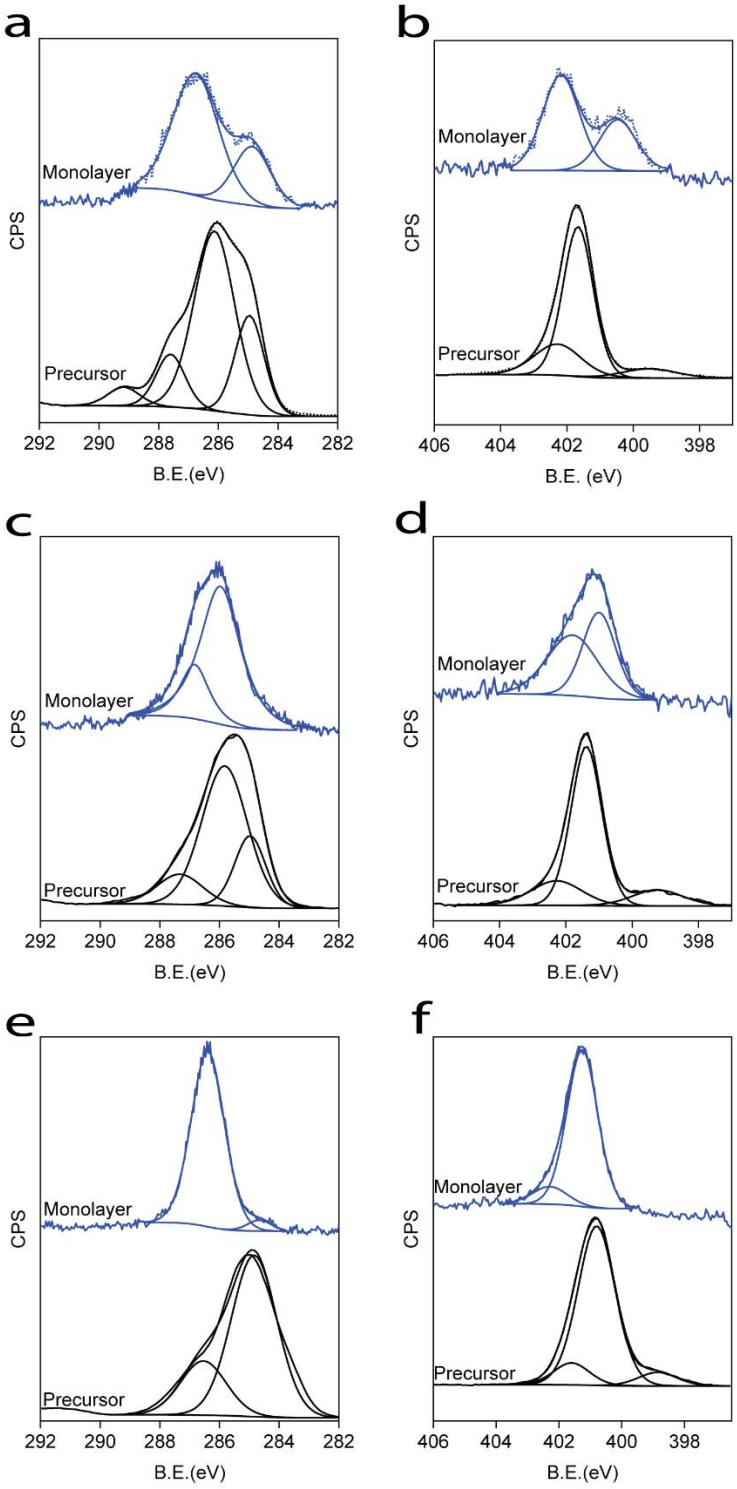

Figure S13. C1s (a,c,e) and N1s (b,d,f) XPS spectra of precursors (black-colored) and self-assembled molecules (blue-colored) of (a,b) NHO-1, (c,d) NHO-2 and (e,f) ^{Me}NHC.

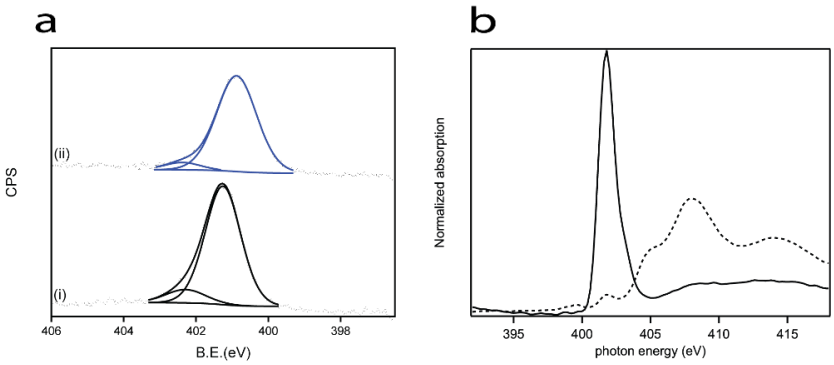

Figure S14. Spectroscopic characterization of ^{Me}NHC SAM. (a) N1s XP-spectra before (i) and after (ii) annealing to 150 °C. (b) Nitrogen K-edge NEXAFS spectra, acquired at p- and s-polarization (marked by solid and dotted lines, respectively).

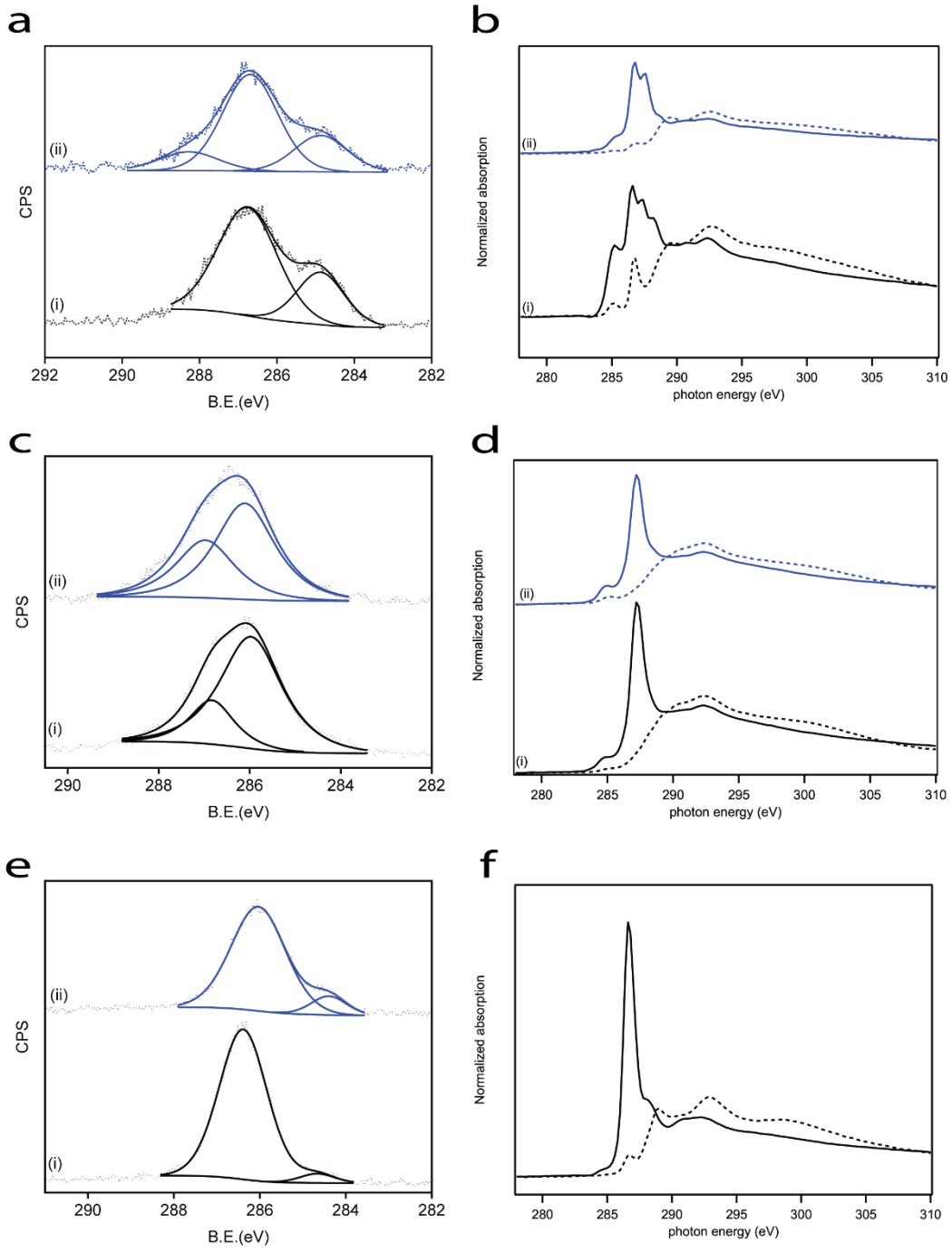

Figure S15. Spectroscopic characterization of NHO-1 (a-b), NHO-2 (c-d) and ^{Me}NHC (e-f) on Au (111), before (i) and after (ii) annealing to 150 °C. C1s XP-spectra (a,c,e) and Carbon K-edge NEXAFS spectra (b,d,f). NEXAFS spectra were acquired at p- and s-polarization (marked by solid and dotted lines, respectively). In the case of NHO-1, the NEXAFS spectra were measured after annealing to 200 °C.

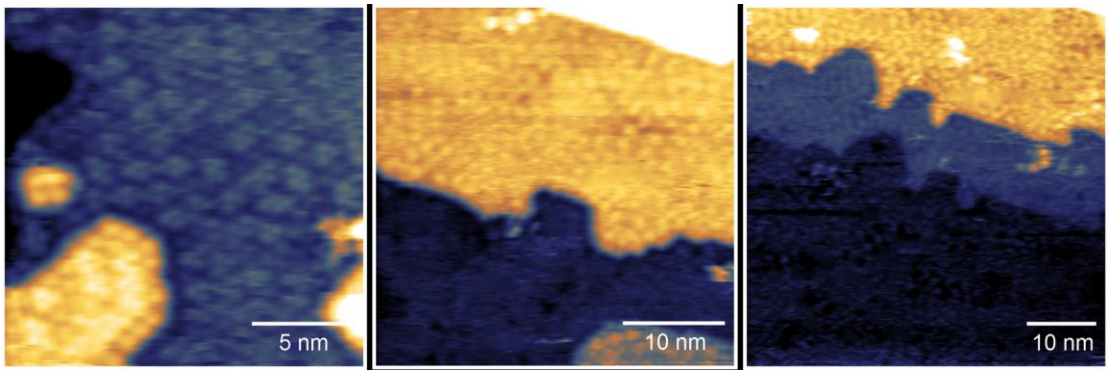

Figure S16. Large-scale images of NHO-2 on Au (111), which were acquired at room temperature (1.6V x 0.3nA).

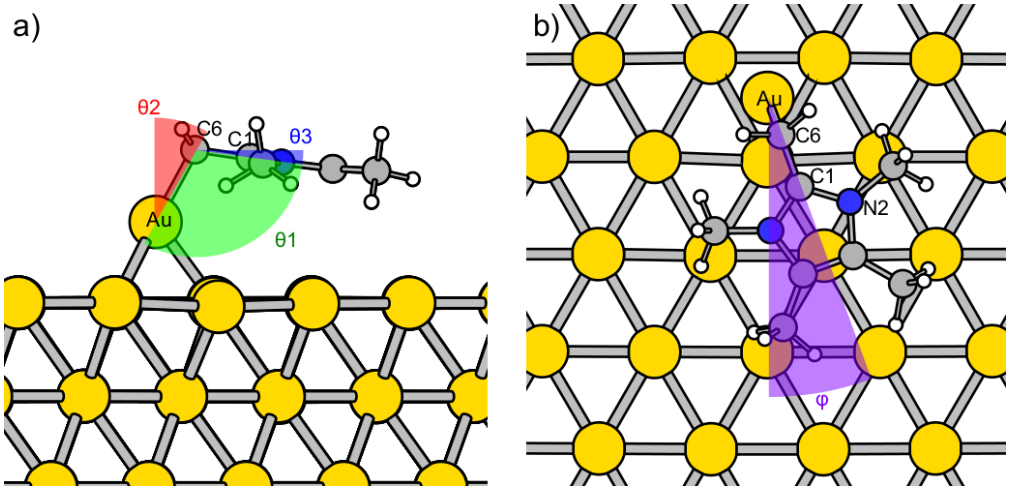

Figure S17. Schematic representation of the atoms and angles as denoted in Table S1.

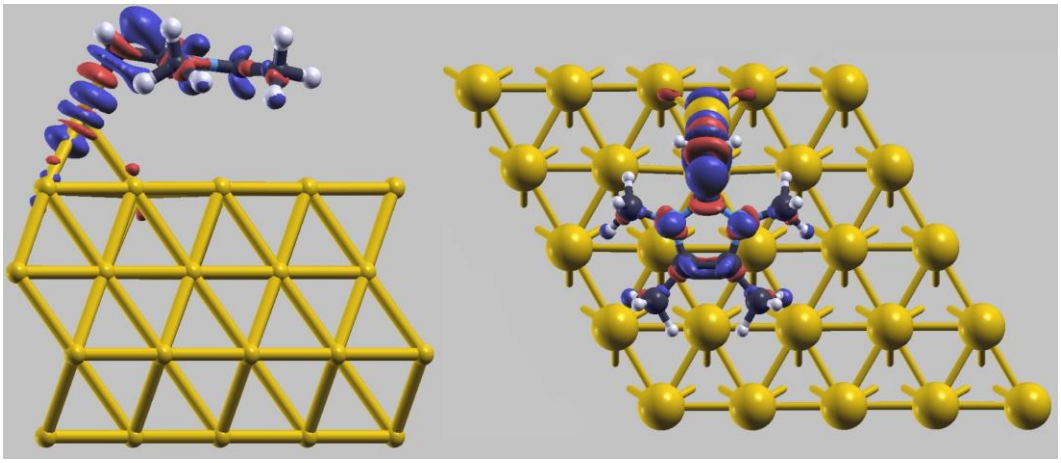

Figure S18. Side (left) and top (right) views of the NHO-2/Au/Au(111), showing the bonding charge density defined as the difference (red = increase, blue = decrease, isovalue = 0.02 $Å^{-3}$) between the charge density of the adsorbed system and those of its constituents, i.e. the surface with an adatom and the molecule. An accumulation of charge density between the C6 atom and the Au adatom can be observed having approximately cylindrical symmetry around the C6-Au bond; within the molecule there is a depletion of π charge and a minor charge accumulation along the σ bonds.

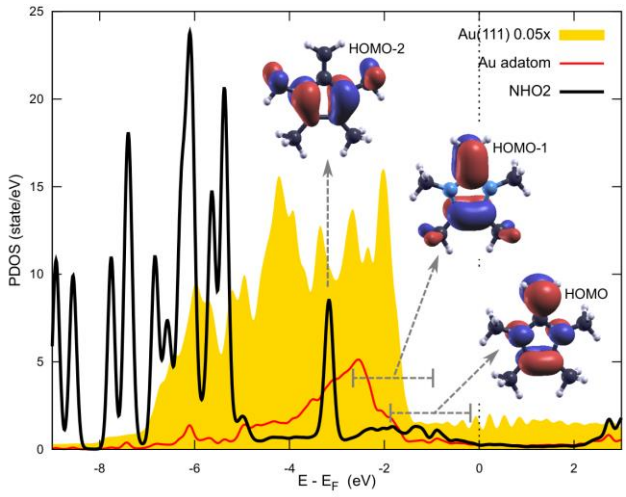

Figure S19. Contributions of the adsorbed NHO-2 molecule (black curve), Au adatom (red curve), Au (111) surface (filled yellow curve) to the electronic density of states (DOS) of NHO-2/Au/Au(111). The energy position and spatial shape of selected frontier orbitals of NHO-2 are shown. NHO-2 HOMO and HOMO-1 orbitals are strongly hybridized with the substrate ones, while the HOMO-2 orbital maintains its molecular character (sharp DOS peak) given its small weight on the CH_2 C-atom, despite the fact that all three orbitals have π symmetry.

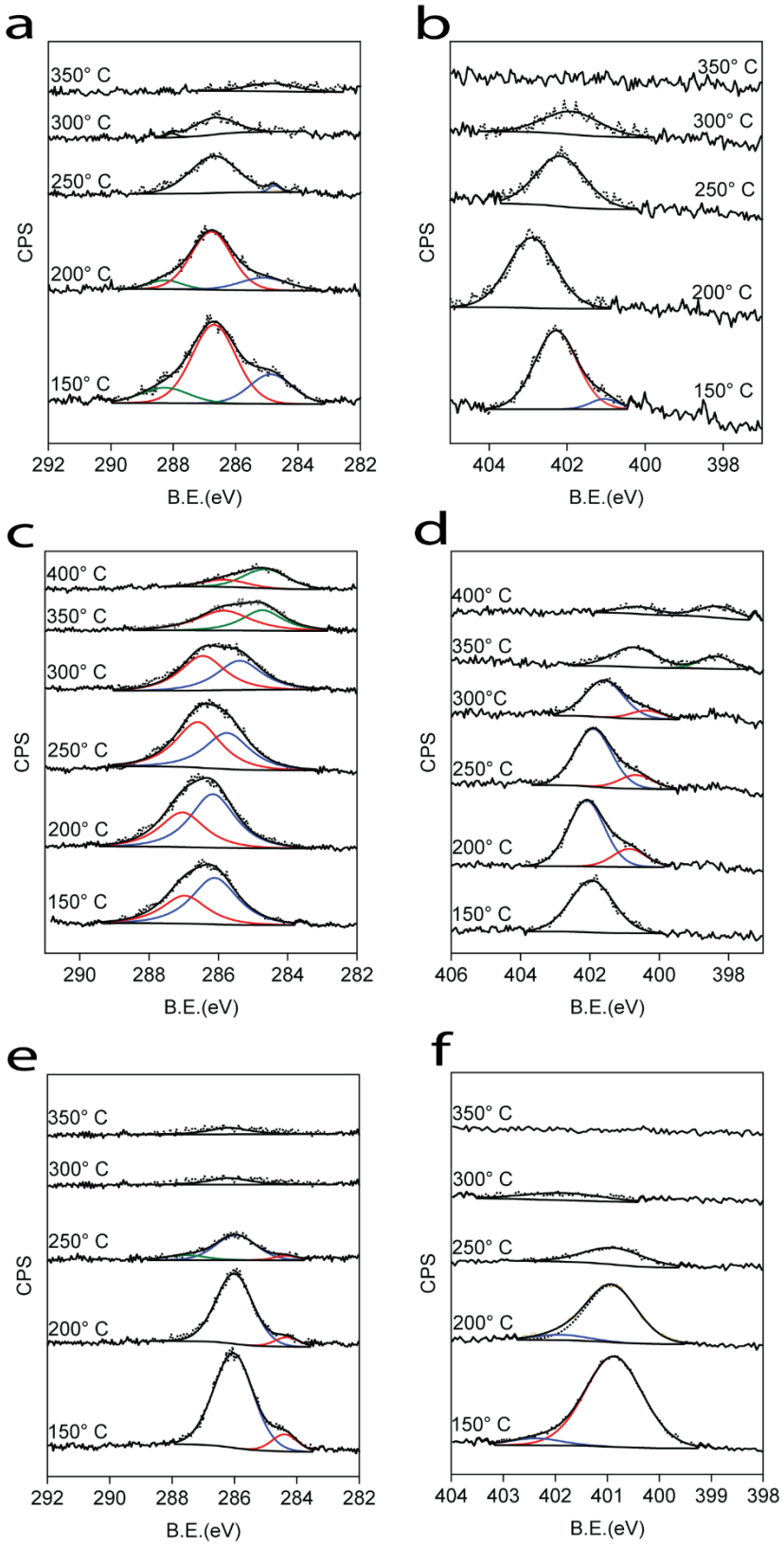

Figure S20. C1s (a,c,e) and N1s (b,d,f) XPS of NHO-1(a,b), NHO-2 (c,d) and ^{Me}NHC (e,f) on Au(111), spectroscopic measurements were conducted following annealing to designated temperatures.

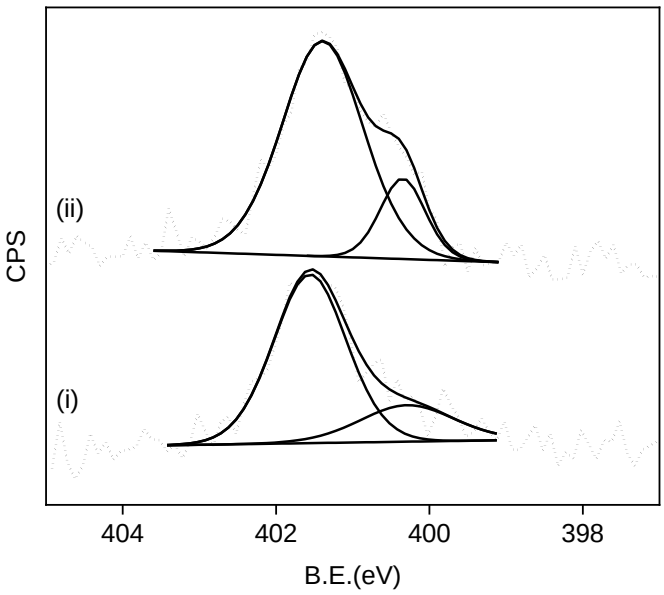

Figure S21. N1s-XPS signal of self-assembled monolayers of NHO-1 (i) and NHO-2 (ii) which were prepared by using 1,2,3 trimethyl imidazolium iodide and 1,2,3,4,5-pentamethyl imidazolium iodide precursors, respectively. Deprotonation was induced by using potassium tert-butoxide and immersing Au-coated Si wafer in the activated NHO solution.

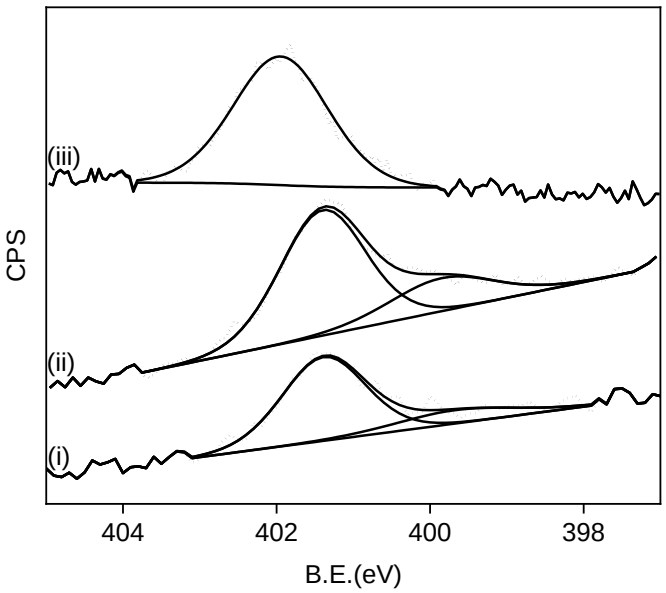

Figure S22. N1s-XPS signal of NHO-2 SAMs on Au film which were prepared by: (i) 1,2,3,4,5-pentamethyl imidazolium iodide precursor that was deprotonated by potassium tert-butoxide in THF; (ii) 1,2,3,4,5-pentamethyl imidazolium hydrogen carbonate precursor that was deprotonated by heating to 70 °C in THF, followed by annealing to 150 °C under N_2; (iii) 1,2,3,4,5-pentamethyl imidazolium hydrogen carbonate precursor that was deprotonated by annealing under UHV conditions. In spectrum (iii), the peak is shifted towards higher binding energies; the shift implies that more positive charge is accumulated on the nitrogen atom in this deposition method, possibly due to differences is the orientation between the deposition methods.

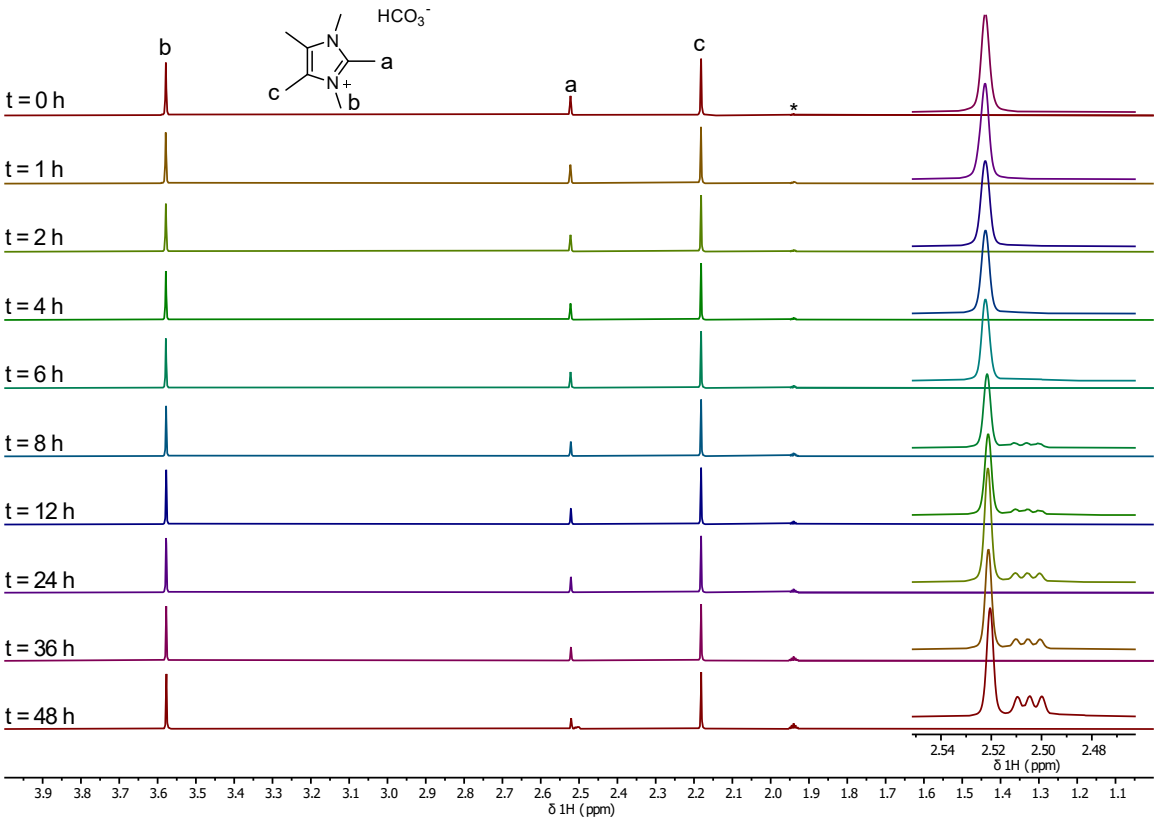

Figure S23. **^{1}H NMR** (501 MHz, CD_3CN, 298 K) stack (asterisk marks solvent). Proton-deuterium exchange at room temperature over 48 h.

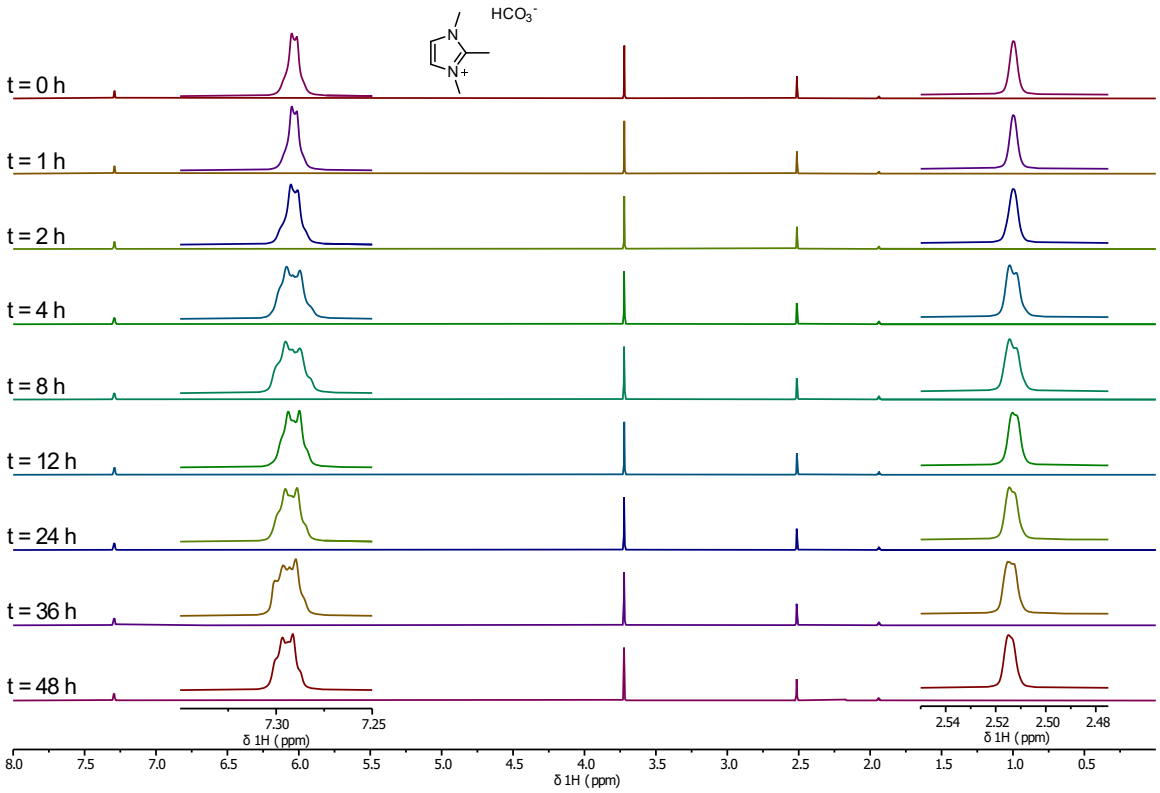

Figure S24. ^{1}H NMR (501 MHz, CD_3CN, 298 K) stack (asterisk marks solvent). Proton-deuterium exchange at room temperature over 48 h.

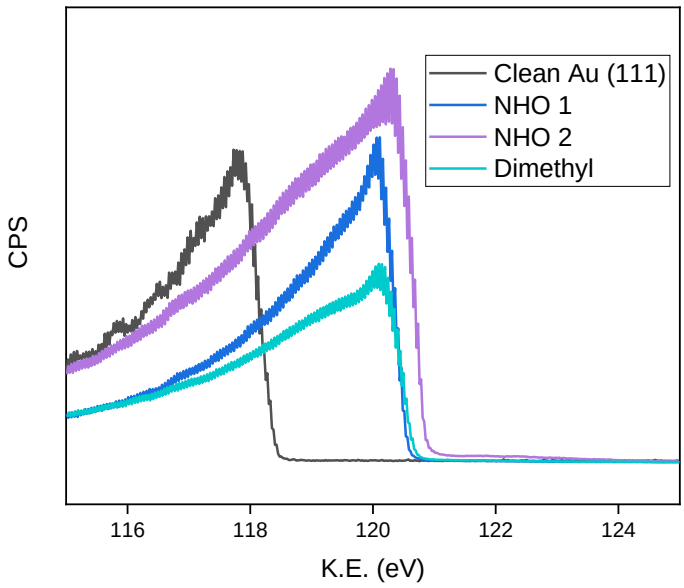

Figure S25. Secondary electrons cut-off used to calculate the work function, taken at a photon energy of 150 eV.

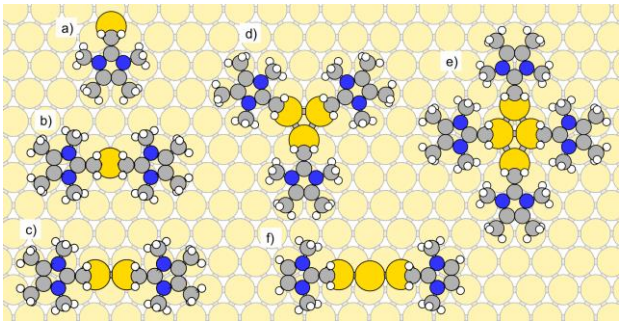

Figure S26. Models of the investigated adsorption configurations: a) a single NHO-2 molecule on an Au adatom, b) two NHO-2 molecules on a single Au adatom, c) two NHO-2 molecules on two adjacent adatoms, i.e a dimer made of two NHO-2-Au-adatom complexes, d) a NHO-2-Au-adatom trimer, e) a NHO-2-Au-adatom tetramer, f) three adjacent Au adatoms, with a NHO-1 molecule adsorbed on each of the two outermost ones.

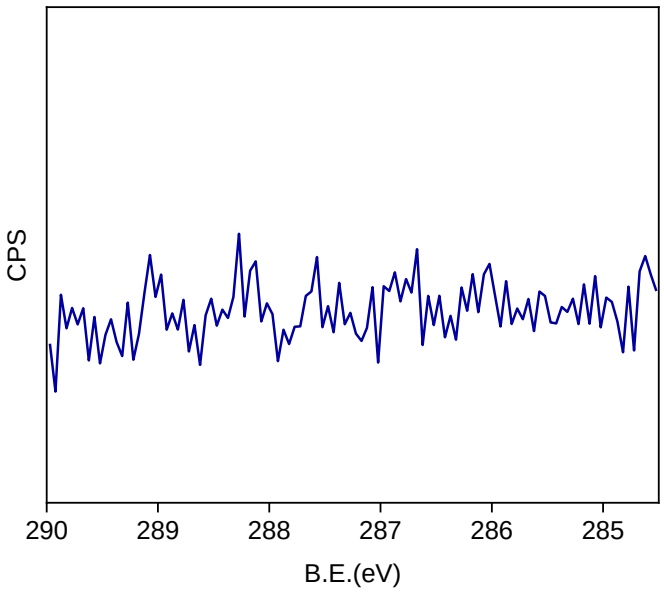

Figure S27. C1s XPS spectrum of Au (111) following sputter-annealing.

SI References

1. Y. B. Wang, Y. M. Wang, W. Z. Zhang, X. B. Lu, *J. Am. Chem. Soc.* **2013**, *135*, 11996–12003.
2. C. M. Crudden, *et al. Nat. Commun.* **2016,** *7*, 12654.
3. M. Smiglak, C. C. Hines, R. D. Rogers, *Green Chem.* **2010**, *12*, 491–501.
4. Z. Li, P. Ji, J. P. Cheng, *J. Org. Chem.* **2021**, *86*, 2974–2985.
5. J. L. Solomon, R. J. Madix, J. Stöhr, *Surf. Sci.* **1991**, *255*, 12–30.
6. P. Giannozzi *et al. J. Phys. Condens. Matter* **2009**, *21*, 395502.
7. P. Giannozzi, *et al.* A*J. Phys. Condens. Matter* **2017,** *29*, 465901.
8. K. F. Garrity, J. W. Bennett, K. M. Rabe, D. Vanderbilt, *Comput. Mater. Sci.* 2014, **2014,** *81*, 446–452.
9. J. Tao, J. P. Perdew, H. Tang, C. Shahi, *J. Chem. Phys.* **2018,** *148*, 74110.
10. S. Ehrlich, J. Moellmann, W. Reckien, T. Bredow, S. Grimme, *ChemPhysChem* **2011**, *12*, 3414–3420.